

# Dark state transport between unitary Fermi superfluids

Mohsen Talebi, Simon Wili, Jeffrey Mohan, Philipp Fabritius,<sup>†</sup> Meng-Zi Huang,<sup>\*</sup> and Tilman Esslinger  
*Institute for Quantum Electronics & Quantum Center, ETH Zürich, 8093 Zürich, Switzerland*  
 (Dated: 2024-06-07)

The formation of dark states is an important concept in quantum sciences, but its compatibility with strong interparticle interactions, for example, in a quantum degenerate gas is hardly explored. Here, we realize a dark state in one of the spins of a two-component, resonantly-interacting Fermi gas using a  $\Lambda$  system within the  $D_2$  transitions of  ${}^6\text{Li}$  at high magnetic field. The dark state is created in a micrometer-sized region within a one-dimensional channel connecting two superfluid reservoirs. The particle transport between the reservoirs is used as a probe. We observe that atoms are transported in the dark state and the superfluid-assisted fast current is preserved. If the dark state resonant condition is not met, the transport is suppressed by the spontaneous emission. We also uncover an asymmetry in the transport timescale across the two-photon resonance, which is absent in the non-interacting regime. This work raises questions on the interplay of dark states with interparticle interactions and opens up perspectives for optical manipulation of fermionic pairing.

*Introduction.*—Dark superposition states are the result of quantum interference in a three-level system [1, 2], also giving rise to the phenomenon of electromagnetically-induced transparency (EIT) [3]. Applications of this concept include quantum memory in atomic media [4–9], compact frequency metrology [10, 11], laser cooling of ultracold atoms and molecules [1, 12, 13], and optical control of Feshbach interactions [14, 15], to name a few. So far, the physics exploited in most systems can be understood at the single-atom or molecule level [16, 17], with few exceptions such as Rydberg dark-state polaritons where many-body interactions lead to optical nonlinearities [18, 19]. However, the interplay between atoms’ internal dark state and their external degrees of freedom in an interacting system in the quantum degenerate regime has been largely unexplored. In particular, in strongly interacting Fermi gases, only molecular dark states which involve fermion pairs as a whole have been realized and studied in regimes where their influence on the many-body pairing at unitarity is still an open question [20].

Here, in a unitary Fermi gas at low temperatures where many-body pairing leads to superfluid behavior, we experimentally realize a dark state in one of the two spins and probe it with transport between two superfluid reservoirs. The dark state is created by optically driving  $\Lambda$ -type transitions locally in a quasi-one-dimensional (quasi-1D) channel connecting the two reservoirs. This configuration therefore protects the superfluid reservoirs from the inevitable residual photon scattering by the  $\Lambda$  couplings. In this strongly interacting system, despite residual atom losses in the channel, we observe superfluid-induced transport as a clear signature of the presence of dark states in the channel. This work opens the toolbox of dark-state engineering for local spin manipulation in strongly interacting fermionic superfluid systems.

*Experimental setup.*—We prepare a balanced mixture of the first and the third hyperfine ground states of  ${}^6\text{Li}$ , with pseudo-spin notations  $|\downarrow\rangle$  and  $|\uparrow\rangle$  respectively. The magnetic field is tuned to the Feshbach resonance at  $B \approx 690$  G of the s-wave collisions between the two

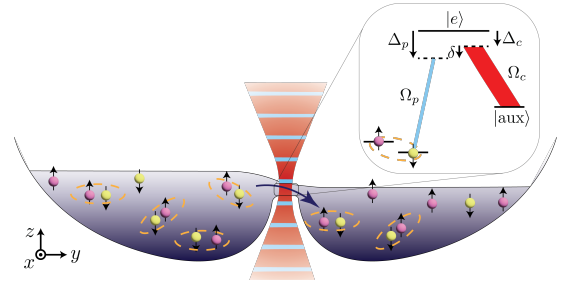


FIG. 1. Transport between two unitary Fermi gas reservoirs in which the connecting channel is locally controlled by a dark state switch acting on spin  $|\downarrow\rangle$ . Two reservoirs containing a balanced mixture of resonantly interacting atoms in states  $|\downarrow\rangle$  and  $|\uparrow\rangle$  are connected via a quasi-1D transport channel. Inside the channel, two beams with a common spatial mode drive a  $\Lambda$  transition (inset), creating a dark state acting like a switch that controls the transport through the channel by the driving fields. The  $\Lambda$  scheme couples the atoms in state  $|\downarrow\rangle$  to an auxiliary state  $|\text{aux}\rangle$  via a two-photon process, with the Rabi couplings and detunings defined in the inset. The interactions between  $|\text{aux}\rangle$  and the two spins are negligible [24].

spins [21]. The gas is confined in a two-reservoir geometry connected via a quantum point contact [22–24] with transverse confinement frequencies 12.3(2) kHz and 10.7(1) kHz along  $x$  and  $z$ , respectively. The transport channel is in the quasi-1D regime since the confinement energy is much higher than the temperature of the cloud  $k_B T/h = 1.67(3)$  kHz where  $k_B$  and  $h$  are the Boltzmann and Planck constants. A schematic of the experimental setup is illustrated in Fig. 1. After preparation of the gas in this geometry, we have a total atom number  $N = N_\downarrow + N_\uparrow = 2.5(2) \times 10^5$  with a degeneracy of  $T/T_F = 0.199(3)$  where  $T_F$  is the Fermi temperature of the gas. See Ref. [24] for more experimental details on the channel’s geometry and the experimental cycle.

We implement a local  $\Lambda$ -scheme inside the 1D channel involving state  $|\downarrow\rangle$  and an auxiliary state  $|\text{aux}\rangle$  (the fifth hyperfine ground state), see Fig. 1. The probe and control couplings are facilitated by two co-propagating

laser beams of the same spatial mode, which are oriented perpendicularly to the transport direction and focused to a waist of 1.5  $\mu\text{m}$  in the channel. In this scheme, a two-photon transition couples the state  $|\downarrow\rangle$  to  $|\text{aux}\rangle$ . The detuning and the effective Rabi frequency averaged over the spatial profile of the probe (control) beam that couples the state  $|\downarrow\rangle$  ( $|\text{aux}\rangle$ ) to an excited state  $|e\rangle$  are denoted with  $\Delta_p$  and  $\Omega_p$  ( $\Delta_c$  and  $\Omega_c$ ) respectively, see the inset of Fig. 1. The dipole matrix element of the probe transition,  $d_p$ , is much smaller than that of the control transition,  $d_c \approx 18.5d_p$ , such that  $\Omega_p \ll \Omega_c$  for comparable intensities. As the two beams are derived from the same laser, their frequency difference is stable on the order of 5 Hz. Due to the opposite sign of the magnetic moments of state  $|\downarrow\rangle$  and  $|\text{aux}\rangle$ , the magnetic field fluctuation which is predominantly at low frequencies (such as 50 Hz), results in an uncertainty of the two-photon detuning  $\delta = \Delta_p - \Delta_c$ . Due to short transit time through the  $\Lambda$  coupling region, each atom only samples the magnetic field noise above 1 kHz (Fourier limit of the transit time). However, the measured signal is sampled from many atoms over seconds and repetitive runs, so is limited by the low-frequency magnetic field noise, leading to a minimally resolved two-photon linewidth  $\sim 80$  kHz [24].

*Dark state resonance by loss spectroscopy.*— We first demonstrate the presence of the dark state resonance by measuring the atom loss as a function of the probe detuning. For this, we prepare the reservoirs at identical thermodynamic conditions and measure the total atom number in each spin after 2 s of illumination of the  $\Lambda$  couplings in the channel. Without the control beam, a resonant probe beam excites  $|\downarrow\rangle$  atoms into  $|e\rangle$  which quickly decay to  $|\text{aux}\rangle$  (since  $d_c \gg d_p$ ) and leave the system, resulting in loss of  $N_\downarrow$ . Scanning the detuning  $\Delta_p$  of a weak probe reveals the broad loss resonance with a linewidth mainly limited by the decay rate of the excited state,  $\Gamma_e \approx 2\pi \times 6$  MHz. With the control beam on and  $\Delta_c \approx 0$ , a peak in  $N_\downarrow$  appears at  $\Delta_p = 0$  due to the existence of a dark state which is decoupled from the laser fields and suppresses the atom loss due to scattering. In Fig. 2 we show the measurements revealing the dark resonance at various choices of  $\Omega_c$ . Here we plot  $N_\downarrow$  normalized to  $N_\uparrow$  to eliminate the effect of shot-to-shot atom number fluctuations which are common to both spins. The observed width of the dark state resonance is limited by the magnetic field noise, as well as the intensity broadening by  $\Omega_p$  and  $\Omega_c$ . By increasing  $\Omega_c$  we observe a broader resonance but also a more robust dark state as is expected also in the absence of collisional interactions [3]. Two additional loss channels affect the observed spectra in  $N_\downarrow/N_\uparrow$ : 1) loss of  $|\uparrow\rangle$  due to the strong interaction between the spins when a  $|\downarrow\rangle$  atom is excited and subsequently lost [35]. 2) pair losses induced by the control beam due to a few off-resonant photoassociation transitions [24].

In our experiment, the photon recoil energy  $E_R \approx k_B \cdot 3.5$   $\mu\text{K}$  is much larger than the trap depth  $U_0 \approx k_B \cdot 1.2$   $\mu\text{K}$ , hence an atom is lost with near-unity probability after a single scattering event. Therefore, an open-system treat-

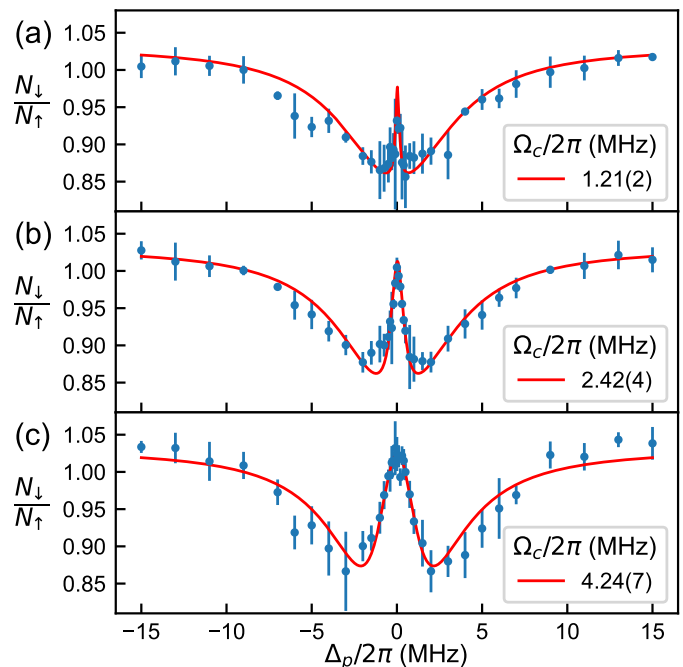


FIG. 2. Atom loss spectroscopy of the dark state resonance in the local  $\Lambda$  coupling configuration of Fig. 1 with balanced reservoirs. We show  $N_\downarrow$  normalized to  $N_\uparrow$  as a function of the detuning of the probe, while the control beam is on resonance  $\Delta_c = 0$ . From (a) to (c), increasing  $\Omega_c$  shows a broader and more robust dark state resonance at the center. Error bars represent standard deviation of typically 4-5 repetitions. Solid lines are the results of a simultaneous fit of a semiclassical model to all measured spectra (three out of six shown here) [24]. In the fit, the common  $\Omega_p$  and all  $\Omega_c$ 's are constrained using the known control-probe power ratios, yielding  $\Omega_p = 2\pi \times 52(1)$  kHz and  $\Omega_c$  shown in each plot [24].

ment is needed to find out how the atoms survive by evolving into the dark state without spontaneous emission, in contrast to the commonly used closed-system treatment [3]. Our model assumes particle loss after each spontaneous emission event [24] using the Monte Carlo wave-function approach [29, 30]. The loss mechanism damps the atoms into the dark state, similar to the process of coherent population trapping [44]. We access the density matrix of a surviving atom by *conditioning* the evolution on no spontaneous emission. Although these atoms do not undergo spontaneous emission, they inherit the projective nature of the emission via the conditioning, similar to the phenomenon of the quantum Zeno effect [33]. We use the steady-state solution of the excited state population from the conditioned evolution to obtain the particle loss rate in the  $\Lambda$  region. A phenomenological model of atoms passing through the  $\Lambda$  region with this loss rate allows us to fit the measured loss spectra (solid lines in Fig. 2). These fits are performed simultaneously for all six measured spectra varying  $\Omega_c$  [24] with three free parameters, including calibration factors of the effective Rabi frequencies and laser frequencies.

Three of these spectra are plotted in Fig. 2. The fit result  $\Omega_p = 2\pi \times 52(1)$  kHz is in good agreement with the measured probe Rabi coupling averaged over the Gaussian waist,  $2\pi \times 58(2)$  kHz [24]. Control  $\Omega_c$ 's are constrained to  $\Omega_p$  in the fit using the measured power ratios and the known ratio of the dipole matrix elements  $d_c/d_p$ . In these spectroscopic measurements, there is no signature of the strong interaction between  $|\downarrow\rangle$  and  $|\uparrow\rangle$  within our measurement precision.

*Probing the dark state with superfluid transport.*—The observed dark state is a coherent superposition of  $|\downarrow\rangle$  and  $|\text{aux}\rangle$ :  $\psi_D \propto \Omega_c |\downarrow\rangle - \Omega_p |\text{aux}\rangle$ , which has a majority population in  $|\downarrow\rangle$  given  $\Omega_c \gg \Omega_p$  in our setting. We now address the question if the pairing between  $|\downarrow\rangle$  and  $|\uparrow\rangle$  in the unitary superfluid is preserved under the local conversion into this dark state. The nature of the gas can be probed by the particle transport between the reservoirs, where superfluidity results in a distinctive non-Ohmic current beyond linear response [23, 40]. We measure the current by first preparing an initial atom number imbalance  $\Delta N$  between the two reservoirs with  $\Delta N/N_0 = 0.27(1)$  ( $N_0$  is the initial total atom number in the cloud). Subsequently, we observe its evolution in time. The relaxation of  $\Delta N/N_0$  for various settings of  $\Omega_p$  and  $\Omega_c$  is presented in Fig. 3(a). In the absence of the local  $\Lambda$  couplings,  $\Omega_p = \Omega_c = 0$ , we observe a fast non-exponential relaxation of the imbalance between the two reservoirs. The corresponding apparent current,  $I = -(1/2) d\Delta N/dt$ , is non-Ohmic, as evidenced by the nonlinear current-bias relation [blue squares in Fig. 3(b)], indicating the superfluid character of the transport process [23]. When we turn on a resonant probe with  $\Omega_p = 2\pi \times 98$  kHz without the control beam, the particle current is reduced and shows Ohmic behavior [orange circles in Fig. 3(a,b)]. This is due to the presence of atom losses in the channel as observed previously [35].

Next, we create the dark state condition in the channel by adding a resonant strong control beam with Rabi coupling  $\Omega_c = 2\pi \times 2.42$  MHz. Now the transport is fast again, with the initial current and the nonlinearity being largely recovered [red triangles in Fig. 3(a,b)]. This observation stands as an evidence for the transport of  $|\downarrow\rangle$  in a dark state while the process largely preserves pairing and the superfluid character. The reduction of the spin-dependent loss is also visible from the time evolution of the  $N_\downarrow/N_\uparrow$  [inset of Fig. 3(a)]. In the final “control” experiment, we only keep on the control beam with the same  $\Omega_c = 2\pi \times 2.42$  MHz while turning off the probe. Despite pair losses induced by the control beam [24], the  $\Delta N$  decay, hence the apparent current, is almost indistinguishable from the case without any  $\Lambda$  coupling [green diamonds in Fig. 3(a,b)]. Therefore, the effect of the pair losses on the apparent current is negligible.

To further investigate the robustness of the dark state transport, we sample a wide range of both the probe and control Rabi frequencies. We determine the initial particle current  $I_0$  with a linear fit to  $\Delta N(t)$  within short transport time  $t \leq 0.08$  s. In Fig. 3(c), we plot  $I_0$  for

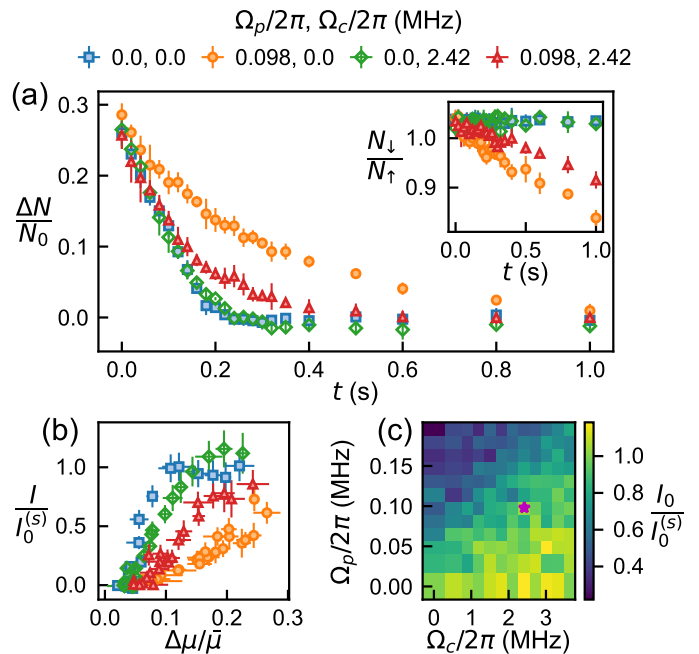


FIG. 3. Dark state recovers superfluid characters of the transport. (a) Time evolution of the particle imbalance for probe and control beam of different strengths. The numerically extracted current-bias relation for the same data are shown in (b). Without any  $\Lambda$  coupling (blue squares), the imbalance shows a fast non-exponential decay, corresponding to a non-Ohmic current-bias relation in (b). With only a resonant probe beam of  $\Omega_p = 2\pi \times 98$  kHz (orange circles), the induced dissipation in the channel leads to a much slower transport as well as an Ohmic current-bias relation. Keeping the same probe and turning on a resonant control  $\Omega_c = 2\pi \times 2.42$  MHz turns  $|\downarrow\rangle$  atoms into the dark state (red triangles). The fast current, as well as its nonlinear characteristics, are recovered to a large extent. The control beam alone (green diamonds) has negligible effect on the transport, only slightly reducing the nonlinearity, visible in (b). (c) Initial current obtained from a linear fit to  $\Delta N(t)$  for transport time  $t \leq 0.08$  s as a function of probe and control Rabi frequencies. All the currents in (b,c) are normalized to that for  $\Omega_p = \Omega_c = 0$ . The magenta star marks the condition for data in (a,b).

combinations of  $\Omega_p$  and  $\Omega_c$ , normalized to  $I_0^s$  that corresponds to the case of  $\Omega_p = \Omega_c = 0$ . For a given choice of  $\Omega_p$ , as we increase  $\Omega_c$ , we observe a trend of increasing initial current, reaching  $I_0^s$ . As we go to higher values of  $\Omega_p$ , higher  $\Omega_c$  is required to maintain a fast transport. At the same time, we observe an increased pair loss by the control beam when its power is increased, which eventually suppresses the current. The configuration for Fig. 3(a,b) is chosen in the intermediate regime [denoted by the star in Fig. 3(c)].

*Asymmetric transport versus two-photon detuning.*—We further investigate the behavior of the transport in terms of the two-photon detuning close to the dark state resonance. We perform the same transport mea-

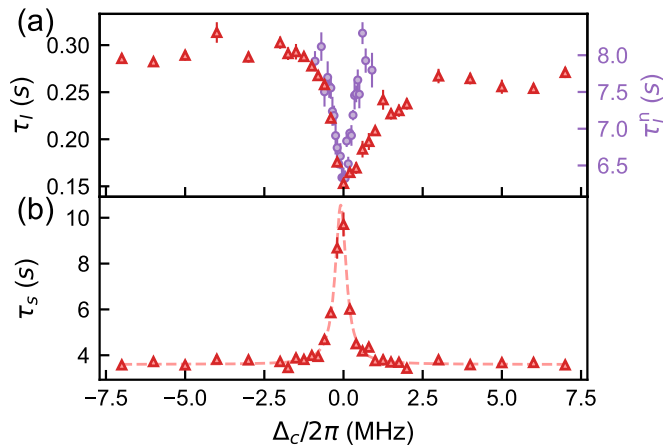


FIG. 4. Observation of asymmetric transport time scale versus two-photon detuning in the unitary gas. (a) The transport time scale as a function of the two-photon detuning (varying  $\Delta_c$  while  $\Delta_p = 0$ ) in the unitary regime (red triangles, left axis), with the same  $\Omega_p$  and  $\Omega_c$  as in Fig. 3(a,b), red triangles. Each point is the time constant  $\tau_I$  of an exponential decay,  $\mathcal{A}e^{-t/\tau_I}$ , fitted to the evolution of the imbalance  $\Delta N/N_0$ , with  $\mathcal{A}$  fixed to the average of all data at  $t = 0$ . We observe that the characteristic transport time of the unitary gas responds asymmetrically to the sign of two-photon detuning. In contrast, a separate measurement in the non-interacting regime (purple circles, right axis) taken under similar  $\Lambda$  couplings [ $\Omega_p = 2\pi \times 112(1)$  kHz,  $\Omega_c = 2\pi \times 2.62(3)$  MHz] does not show such asymmetry. Time constants  $\tau_I^{\dagger}$  for the non-interacting regime are obtained in the same way as  $\tau_I$  but fitting  $\Delta N_i/N_{\dagger}$  where  $N_{\dagger}$  simply serves as a precise estimate of  $N_{\dagger}(0)$ . (b) The corresponding loss rate versus two-photon detuning in the unitary regime shows no asymmetry [same data as the red triangles in (a)]. The time constants  $\tau_s$  are obtained from exponential fits  $\bar{s}_0 e^{-t/\tau_s}$  to the spin ratio  $s = N_{\downarrow}/N_{\uparrow}$ , with  $\bar{s}_0$  fixed to the average of all data at  $t = 0$ . The dashed line is a Lorentzian fit as a guide to the eye. Error bars represent standard errors from the fits.

surement as above with a detuned control frequency  $\Delta_c \in 2\pi \times [-7, 7]$  MHz while keeping the probe frequency on the single photon resonance ( $\Delta_p = 0$ ). The effective Rabi couplings  $\Omega_p$  and  $\Omega_c$  are chosen the same as previously in Fig. 3(a), red triangles. We characterize the transport by the time scale  $\tau_I$  obtained from an exponential fit to  $\Delta N/N_0$ . The results versus the control detuning are shown in Fig. 4(a), red triangles. Here, we observe a clearly visible asymmetry of the characteristic transport times across the resonance: the particle imbalance relaxes faster for  $\Delta_c > 0$  than  $\Delta_c < 0$  for a given  $|\Delta_c|$  near resonance. However, we do not observe such a behavior in the atom loss rate, which is symmetric with respect to  $\Delta_c$  as characterized by the decay of the spin ratio  $s(t) = N_{\downarrow}(t)/N_{\uparrow}(t)$  (as used in Fig. 2). This is visible from exponential-decay fits to  $s(t)$ , whose decay times  $\tau_s$  are plotted versus  $\Delta_c$  in Fig. 4(b). At the single-atom level, a possible origin of an asymmetry is the dispersive asymmetry in the local conservative po-

tential of the  $\Lambda$ -coupling away from the two-photon resonance. The observed asymmetry suggests a repulsive (attractive) potential with a negative (positive)  $\Delta_c$ , resulting in a slower (faster) transport. However, within our conditioned evolution description, atoms experience a negligible net light shift in the steady state [24]. Furthermore, the simulated transient evolution before reaching the steady state shows that the light shift is maximally  $4 \text{ nK} \cdot k_B$  for the explored range of  $\Delta_c$ , negligible compared to any relevant energy scales such as the temperature ( $\sim 80 \text{ nK}$ ) or Fermi energy ( $\sim 400 \text{ nK} \cdot k_B$ ). Our theory of three-level single-particle light-matter interaction does not seem to explain the observed asymmetry, yet it is consistent with a separate measurement in the non-interacting regime where we do not observe such an asymmetry [purple circles in Fig. 4(a)]. In principle, the asymmetry could still originate from single-particle behavior but is too small to measure in the non-interacting regime while the superfluid-enhanced current amplifies the subtle effect. One possible mechanism could be non-adiabatic conservative potentials [45] during the transient atomic evolution before reaching the steady state.

On the other hand, the asymmetry observed only in the unitary gas could also have a many-body origin. One possible mechanism to introduce an asymmetry is the pairing between  $|\downarrow\rangle$  and  $|\uparrow\rangle$ , similar to the asymmetric rf spectrum of the pairing gap [46–48]. Here, the  $\Lambda$  scheme couples the resonantly interacting  $|\downarrow\rangle - |\uparrow\rangle$  pairs to the free  $|\text{aux}\rangle - |\uparrow\rangle$  pairs. The pairing between  $|\downarrow\rangle$  and  $|\uparrow\rangle$  leads to nonzero two-photon coupling to a broad continuum of relative momentum states of the free pairs for  $\Delta_c > 0$ , effectively broadening the dark state resonance on the  $\Delta_c > 0$  side. This picture is consistent with the observed faster transport at  $\Delta_c > 0$ , but also predicts an asymmetry in the atom loss. If the latter should exist below our experimental resolution [Fig. 4(b)], it would suggest that the superfluid-enhanced transport in the unitary gas is a sensitive probe of subtle many-body effects. A detailed study of these scenarios goes beyond the scope of this work as it requires new approaches or extending the theoretical studies on interacting fermions in spin-dependent  $\Lambda$  schemes [49–52] to transport settings.

*Conclusion.*— In this work, we reported on an experimental realization of a spin-selective dark state inside a 1D channel connecting two fermionic unitary superfluid reservoirs. We observed a revival of the non-ohmic current-bias characteristic as a result of the dark state transport through the channel. Furthermore, we observed an asymmetric dependence of the characteristic transport time on the two-photon detuning. This asymmetry is not observed in the non-interacting regime, suggesting that a full explanation might require taking into account many-body effects. Our work paves the way for studying dark states in the strongly interacting regime and their interplay with superfluid transport phenomena.



## ACKNOWLEDGMENTS

We thank Alexander Frank for technical support. We are grateful for discussions with Alex Gómez Salvador and Eugene Demler. We also thank Ran Qi for sharing

his calculation of the scattering lengths. We acknowledge the Swiss National Science Foundation (Grants No. 212168, UeM019-5.1, 182650, and TMAG-2 209376) and European Research Council advanced grant TransQ (Grant No. 742579) for funding.

<sup>†</sup> Present address: X-Rite Europe GmbH, Regensdorf, Switzerland

\* Corresponding author: [mhuang@phys.ethz.ch](mailto:mhuang@phys.ethz.ch)

- [1] C. Cohen-Tannoudji, Dark resonances from optical pumping to cold atoms and molecules, *Physica Scripta* **90**, 088013 (2015).
- [2] G. Alzetta, A. Gozzini, L. Moi, and G. Orriols, An experimental method for the observation of r.f. transitions and laser beat resonances in oriented Na vapour, *Il Nuovo Cimento B Series 11* **36**, 5 (1976).
- [3] M. Fleischhauer, A. Imamoglu, and J. P. Marangos, Electromagnetically induced transparency: Optics in coherent media, *Reviews of Modern Physics* **77**, 633 (2005).
- [4] A. I. Lvovsky, B. C. Sanders, and W. Tittel, Optical quantum memory, *Nature Photonics* **3**, 706 (2009).
- [5] M. Fleischhauer and M. D. Lukin, Dark-State Polaritons in Electromagnetically Induced Transparency, *Physical Review Letters* **84**, 5094 (2000).
- [6] C. Liu, Z. Dutton, C. H. Behroozi, and L. V. Hau, Observation of coherent optical information storage in an atomic medium using halted light pulses, *Nature* **409**, 490 (2001).
- [7] D. F. Phillips, A. Fleischhauer, A. Mair, R. L. Walsworth, and M. D. Lukin, Storage of Light in Atomic Vapor, *Physical Review Letters* **86**, 783 (2001).
- [8] Y. Wang, J. Li, S. Zhang, K. Su, Y. Zhou, K. Liao, S. Du, H. Yan, and S.-L. Zhu, Efficient quantum memory for single-photon polarization qubits, *Nature Photonics* **13**, 346 (2019).
- [9] M. Cao, F. Hoffet, S. Qiu, A. S. Sheremet, and J. Laurat, Efficient reversible entanglement transfer between light and quantum memories, *Optica* **7**, 1440 (2020).
- [10] V. Shah and J. Kitching, Advances in coherent population trapping for atomic clocks, in *Advances in atomic, molecular, and optical physics*, Vol. 59 (Elsevier, 2010) pp. 21–74.
- [11] S. Knappe, MEMS Atomic Clocks, in *Comprehensive Microsystems* (Elsevier, 2008) pp. 571–612.
- [12] E. Arimondo, V coherent population trapping in laser spectroscopy, in *Progress in optics*, Vol. 35, edited by E. Wolf (Elsevier, 1996) pp. 257–354.
- [13] K.-K. Ni, S. Ospelkaus, M. H. G. de Miranda, A. Pe’er, B. Neyenhuis, J. J. Zirbel, S. Kotochigova, P. S. Julienne, D. S. Jin, and J. Ye, A High Phase-Space-Density Gas of Polar Molecules, *Science* **322**, 231 (2008).
- [14] G. Thalhammer, M. Theis, K. Winkler, R. Grimm, and J. H. Denschlag, Inducing an optical Feshbach resonance via stimulated Raman coupling, *Physical Review A* **71**, 033403 (2005).
- [15] A. Jagannathan, N. Arunkumar, J. A. Joseph, and J. E. Thomas, Optical Control of Magnetic Feshbach Resonances by Closed-Channel Electromagnetically Induced Transparency, *Physical Review Letters* **116**, 075301 (2016).
- [16] K. Winkler, G. Thalhammer, M. Theis, H. Ritsch, R. Grimm, and J. H. Denschlag, Atom-Molecule Dark States in a Bose-Einstein Condensate, *Physical Review Letters* **95**, 063202 (2005).
- [17] H. Wu and J. E. Thomas, Optical Control of Feshbach Resonances in Fermi Gases Using Molecular Dark States, *Physical Review Letters* **108**, 010401 (2012).
- [18] C. S. Hofmann, G. Günter, H. Schempp, M. Robert-de Saint-Vincent, M. Gärtner, J. Evers, S. Whitlock, and M. Weidemüller, Sub-Poissonian Statistics of Rydberg-Interacting Dark-State Polaritons, *Physical Review Letters* **110**, 203601 (2013).
- [19] E. Zeuthen, M. J. Gullans, M. F. Maghrebi, and A. V. Gorshkov, Correlated Photon Dynamics in Dissipative Rydberg Media, *Physical Review Letters* **119**, 043602 (2017).
- [20] M. Semczuk, W. Gunton, W. Bowden, and K. W. Madison, Anomalous Behavior of Dark States in Quantum Gases of <sup>6</sup>Li, *Physical Review Letters* **113**, 055302 (2014).
- [21] G. Zürn, T. Lompe, A. N. Wenz, S. Jochim, P. S. Julienne, and J. M. Hutson, Precise characterization of <sup>6</sup>Li feshbach resonances using trap-sideband-resolved rf spectroscopy of weakly bound molecules, *Phys. Rev. Lett.* **110**, 135301 (2013).
- [22] S. Krinner, D. Stadler, D. Husmann, J.-P. Brantut, and T. Esslinger, Observation of quantized conductance in neutral matter, *Nature* **517**, 64 (2014).
- [23] D. Husmann, S. Uchino, S. Krinner, M. Lebrat, T. Gimarchi, T. Esslinger, and J.-P. Brantut, Connecting strongly correlated superfluids by a quantum point contact, *Science* **350**, 1498 (2015).
- [24] See Supplemental Material at [URL will be inserted by publisher] for additional information on the theoretical methods, experimental procedures and data analysis, which includes Ref. [3,25-43].
- [25] W. I. McAlexander, E. R. I. Abraham, and R. G. Hulet, Radiative lifetime of the 2 P state of lithium, *Physical Review A* **54**, R5 (1996).
- [26] F. Renzoni, W. Maichen, L. Windholz, and E. Arimondo, Coherent population trapping with losses observed on the Hanle effect of the *D*<sub>1</sub> sodium line, *Physical Review A* **55**, 3710 (1997).
- [27] F. Renzoni and E. Arimondo, Population-loss-induced narrowing of dark resonances, *Physical Review A* **58**, 4717 (1998).
- [28] F. Renzoni, A. Lindner, and E. Arimondo, Coherent population trapping in open systems: A coupled/noncoupled-state analysis, *Physical Review A* **60**, 450 (1999).
- [29] J. Dalibard, Y. Castin, and K. Mølmer, Wave-function approach to dissipative processes in quantum optics, *Physical Review Letters* **68**, 580 (1992).

- [30] K. Mølmer, Y. Castin, and J. Dalibard, Monte Carlo wave-function method in quantum optics, *Journal of the Optical Society of America B* **10**, 524 (1993).
- [31] M. A. Nielsen and I. L. Chuang, *Quantum computation and quantum information* (Cambridge university press, 2010).
- [32] J. Skinner and D. Hsu, Pure dephasing of a two-level system, *The Journal of Physical Chemistry* **90**, 4931 (1986).
- [33] E. W. Streed, J. Mun, M. Boyd, G. K. Campbell, P. Medley, W. Ketterle, and D. E. Pritchard, Continuous and Pulsed Quantum Zeno Effect, *Physical Review Letters* **97**, 260402 (2006).
- [34] J. Johansson, P. Nation, and F. Nori, QuTiP: An open-source Python framework for the dynamics of open quantum systems, *Computer Physics Communications* **183**, 1760 (2012).
- [35] M.-Z. Huang, J. Mohan, A.-M. Visuri, P. Fabritius, M. Talebi, S. Wili, S. Uchino, T. Giamarchi, and T. Esslinger, Superfluid Signatures in a Dissipative Quantum Point Contact, *Physical Review Letters* **130**, 200404 (2023).
- [36] M. Bartenstein, A. Altmeyer, S. Riedl, R. Geursen, S. Jochim, C. Chin, J. H. Denschlag, R. Grimm, A. Simoni, E. Tiesinga, C. J. Williams, and P. S. Julienne, Precise Determination of Li 6 Cold Collision Parameters by Radio-Frequency Spectroscopy on Weakly Bound Molecules, *Physical Review Letters* **94**, 103201 (2005).
- [37] C. Chin, R. Grimm, P. Julienne, and E. Tiesinga, Feshbach resonances in ultracold gases, *Reviews of Modern Physics* **82**, 1225 (2010).
- [38] F. A. Van Abeelen, B. J. Verhaar, and A. J. Moerdijk, Sympathetic cooling of Li 6 atoms, *Physical Review A* **55**, 4377 (1997).
- [39] X. Li, S. Wang, X. Luo, Y.-Y. Zhou, K. Xie, H.-C. Shen, Y.-Z. Nie, Q. Chen, H. Hu, Y.-A. Chen, X.-C. Yao, and J.-W. Pan, Observation and quantification of the pseudogap in unitary Fermi gases, *Nature* **626**, 288 (2024).
- [40] P. Fabritius, J. Mohan, M. Talebi, S. Wili, W. Zwerger, M.-Z. Huang, and T. Esslinger, Irreversible entropy transport enhanced by fermionic superfluidity, *Nature Physics* **10.1038/s41567-024-02483-3** (2024).
- [41] M. E. Gehm, *Preparation of an optically-trapped degenerate Fermi gas of  $^6\text{Li}$ : Finding the route to degeneracy* (Duke University, 2003).
- [42] K. M. Jones, E. Tiesinga, P. D. Lett, and P. S. Julienne, Ultracold photoassociation spectroscopy: Long-range molecules and atomic scattering, *Reviews of Modern Physics* **78**, 483 (2006).
- [43] G. B. Partridge, K. E. Strecker, R. I. Kamar, M. W. Jack, and R. G. Hulet, Molecular Probe of Pairing in the BEC-BCS Crossover, *Physical Review Letters* **95**, 020404 (2005).
- [44] B. W. Shore, *The Theory of Coherent Atomic Excitation: Multilevel Atoms and Incoherence* (Wiley, New York, 1990).
- [45] R. Dum and M. Olshanii, Gauge Structures in Atom-Laser Interaction: Bloch Oscillations in a Dark Lattice, *Physical Review Letters* **76**, 1788 (1996).
- [46] C. Chin, M. Bartenstein, A. Altmeyer, S. Riedl, S. Jochim, J. H. Denschlag, and R. Grimm, Observation of the pairing gap in a strongly interacting fermi gas, *Science* **305**, 1128 (2004).
- [47] C. Chin and P. S. Julienne, Radio-frequency transitions on weakly bound ultracold molecules, *Physical Review A* **71**, 012713 (2005).
- [48] C. H. Schunck, Y.-i. Shin, A. Schirotzek, and W. Ketterle, Determination of the fermion pair size in a resonantly interacting superfluid, *Nature* **454**, 739 (2008).
- [49] T.-L. Dao, A. Georges, J. Dalibard, C. Salomon, and I. Carusotto, Measuring the One-Particle Excitations of Ultracold Fermionic Atoms by Stimulated Raman Spectroscopy, *Physical Review Letters* **98**, 240402 (2007).
- [50] L. Jiang, H. Pu, W. Zhang, and H. Y. Ling, Detection of Fermi pairing via electromagnetically induced transparency, *Physical Review A* **80**, 033606 (2009).
- [51] L. Zhou, K. Zhang, B. Zhu, Y. Li, and W. Zhang, Phase detection in an ultracold polarized Fermi gas via electromagnetically induced transparency, *Physics Letters A* **376**, 919 (2012).
- [52] H. H. Jen and D.-W. Wang, Theory of electromagnetically induced transparency in strongly correlated quantum gases, *Physical Review A* **87**, 061802 (2013).

## SUPPLEMENTAL MATERIAL

### I. FORMALISM OF THREE-LEVEL SYSTEM WITH PARTICLE LOSS

In this section, we formulate the system's density matrix under  $\Lambda$  coupling while taking into account atom loss due to the recoil of photon scattering. This is done by considering two subspaces of external states, one surviving and one lost, and the jump processes between them. We arrive at the nonlinear evolution equation of the surviving atoms. On the one hand, we use a numerical method to extract the state of the surviving atoms for an arbitrary time. On the other hand, we analytically solve for the steady state of this evolution, which is later used in fitting the measured spectra.

#### A. Derivation of the state evolution of a surviving atom

The  $\Lambda$  system we use couples the first ( $|\downarrow\rangle = |1\rangle$ ) and the fifth ( $|\text{aux}\rangle = |5\rangle$ ) hyperfine ground states to a common excited state  $|e\rangle = |2P_{3/2}, m_J = 3/2, m_I = 0\rangle$  using two  $\sigma_+$  polarized beams with a common spatial mode in the  $D_2$  transition manifold. The total decay rate of the excited state is  $\Gamma_e = 2\pi \times 5.87$  MHz [25] with dominant decay rates to  $|1\rangle$  and  $|5\rangle$  of  $\Gamma_{e1} \approx 2.9 \times 10^{-3}\Gamma_e$  and  $\Gamma_{e5} \approx 0.997\Gamma_e$ , respectively. The total spontaneous decay rate to other states is  $\sim 8 \times 10^{-7}\Gamma_e$  so that we can neglect atomic transitions outside the  $|1\rangle - |e\rangle - |5\rangle$  system.

In our experimental condition, a comparison of the recoil energy  $E_r = \hbar^2 k^2 / (2m) \approx k_B \cdot 3.5$   $\mu\text{K}$  and the trap depth  $U_0 \approx k_B \cdot 1.2$   $\mu\text{K}$  shows that an atom is lost with a high chance after a single spontaneous emission event. Therefore, the evolution of the surviving atoms in the cloud needs to be modeled by considering a loss channel outside of the  $\Lambda$  system. As discussed in [26–28], the behavior of the coherent population trapping in the dark state can be influenced dramatically by such a loss process. To model such a loss mechanism, we adapt the physical picture of gedanken projective measurements in the Monte Carlo wavefunction (MCWF) approach [29, 30] and simultaneously model the internal and external degrees of freedom of a single atom. As we detail below, the major difference of our derivation compared to the Refs. [29, 30] lies in *conditioning* the survival of an atom on the absence of spontaneous emission. We will show that this assumption results in a nonlinear master equation of the survived atoms.

Assume that the atom is in the pure product state  $|\psi\rangle = |\phi_{\text{int}}\rangle \otimes |\phi_{\text{ext}}\rangle$  where  $|\phi_{\text{int}}\rangle$  and  $|\phi_{\text{ext}}\rangle$  denote the internal atomic and external motional states. We classify the external state in two categories:

$$S_{\text{in}} = \text{span} \{ |\mathbf{p}\rangle : |\mathbf{p}| < p_c \}, \quad (1)$$

$$S_{\text{out}} = \text{span} \{ |\mathbf{p}\rangle : |\mathbf{p}| > p_c \}, \quad (2)$$

where  $S_{\text{in}}$  is the set of states that survive in the  $\Lambda$  region while  $S_{\text{out}}$  is the set of states that are eventually lost from the trap. Here, we assume that an atom is lost from the trap if it has a momentum higher than the critical momentum  $p_c$  determined by the trap depth  $p_c \sim \sqrt{2mU_0}$ . Since the recoil momentum  $\hbar k$  is much larger than  $p_c$ , we assume that a spontaneous emission event transfers an atom initially in  $S_{\text{in}}$  to  $S_{\text{out}}$ .

Assume that the state of the atom at time  $t$  is  $|\Psi(t)\rangle = |\phi_{\text{int}}(t)\rangle \otimes |\phi_{\text{ext}}^{(\text{in})}(t)\rangle$  in which  $|\phi_{\text{int}}(t)\rangle = \alpha_1|1\rangle + \alpha_5|5\rangle + \alpha_e|e\rangle$  and  $|\phi_{\text{ext}}^{(\text{in})}(t)\rangle \in S_{\text{in}}$ . The Hermitian part of the evolution in the  $\Lambda$  region is governed by the Hamiltonian  $\hat{H} = \hat{H}_\Lambda \otimes \hat{\Pi}_{\text{in}} + \hat{H}'_\Lambda \otimes \hat{\Pi}_{\text{out}}$  in which  $\hat{\Pi}_{\text{in}}$  ( $\hat{\Pi}_{\text{out}}$ ) is the projection operator into  $S_{\text{in}}$  ( $S_{\text{out}}$ ). While  $\hat{H}'_\Lambda$  might differ from  $\hat{H}_\Lambda$ , only the latter, the light-matter Hamiltonian of the surviving atoms, is relevant in the following. The Hamiltonian  $\hat{H}_\Lambda$  in the rotating frame with rotating wave-approximation reads

$$\hat{H}_\Lambda = -\frac{\hbar}{2} \begin{pmatrix} 0 & 0 & \Omega_p \\ 0 & -2(\Delta_p - \Delta_c) & \Omega_c \\ \Omega_p & \Omega_c & -2\Delta_p \end{pmatrix}, \quad (3)$$

where  $\Delta_p = \omega_{1e} - \omega_p$  and  $\Delta_c = \omega_{5e} - \omega_c$  denote the probe and control detuning respectively, and  $\omega_p$  and  $\omega_c$  are the laser frequencies and  $\omega_{1e}$  and  $\omega_{5e}$  are the frequencies of the corresponding atomic transitions. Furthermore in (3), the Rabi couplings of the probe and control for the survived atoms in  $S_{\text{in}}$  are denoted by  $\Omega_p$  and  $\Omega_c$  respectively.

#### Jump processes and probabilities

During a differential time evolution  $dt$ , we consider the following Markovian jump processes in the framework of MCWF:

1. Spontaneous emission from  $|e\rangle$  to  $|5\rangle$  or  $|1\rangle$  with jump operators

$$\hat{S}_{e5}^{\text{spon}} = \sqrt{\Gamma_{e5}} |5\rangle \langle e| \otimes |\phi_{\text{ext}}^{(\text{out})}(t)\rangle \langle \phi_{\text{ext}}^{(\text{in})}(t)|, \quad (4)$$

$$\hat{S}_{e1}^{\text{spon}} = \sqrt{\Gamma_{e1}} |1\rangle \langle e| \otimes |\phi_{\text{ext}}^{(\text{out})}(t)\rangle \langle \phi_{\text{ext}}^{(\text{in})}(t)|, \quad (5)$$

which simultaneously change the external state of the atom to  $|\phi_{\text{ext}}^{(\text{out})}(t)\rangle \in S_{\text{out}}$  encoding the particle loss due to the spontaneous emission. These jump processes occur with probabilities  $dp_{e5}^{\text{spon}} = dt \langle \Psi | (\hat{S}_{e5}^{\text{spon}})^\dagger \hat{S}_{e5}^{\text{spon}} | \Psi \rangle = \Gamma_{e5} |\alpha_e|^2 dt$  and  $dp_{e1}^{\text{spon}} = dt \langle \Psi | (\hat{S}_{e1}^{\text{spon}})^\dagger \hat{S}_{e1}^{\text{spon}} | \Psi \rangle = \Gamma_{e1} |\alpha_e|^2 dt$ , respectively, during a differential time evolution  $dt$ .

2. Dephasing due to fluctuations of the two-photon detuning  $\delta = \Delta_p - \Delta_c$ . In our experiment, the major source of this non-Hermitian process is the magnetic field noise. From the Hamiltonian (3), the Markovian fluctuations in the two-photon detuning will result in random phase kicks [31] modelled

by a jump operator of the form [3, 30]

$$\hat{\mathcal{S}}_5^{\text{deph}} = \sqrt{\gamma_5}|5\rangle\langle 5| \otimes \hat{I}^{\text{ext}}, \quad (6)$$

which projects the internal state to  $|5\rangle$  while not influencing the external state as a result of the identity operator  $\hat{I}^{\text{ext}}$ . We assume that the two-photon detuning is of the form  $\delta = \tilde{\delta} + \eta(t)$  in which  $\tilde{\delta}$  is the average value and  $\eta(t)$  is sampled from a white Gaussian noise with zero mean. With this assumption, we can show that the system undergoes the jump process (6) if the auto-correlation function of the white noise is set to  $\langle \eta(t)\eta(t') \rangle = \gamma_5 \delta_D(t - t')$  with  $\delta_D$  denoting the Dirac's  $\delta$ -function [32]. The probability of an occurrence of the jump during the differential time  $dt$  is  $dp_5^{\text{deph}} = dt \langle \Psi | (\hat{\mathcal{S}}_5^{\text{deph}})^\dagger \hat{\mathcal{S}}_5^{\text{deph}} | \Psi \rangle = \gamma_5 |\alpha_5|^2 dt$ . We mention that this dephasing process results in a reduction of the peak value of the EIT spectrum for small enough  $\Omega_p$  and  $\Omega_c$  [see Fig. 2(a)]. Furthermore, in cases that this dephasing process is the limiting factor ( $\Omega_p \ll \Omega_c \sim \gamma_5$ ),  $\gamma_5$  describes the full width at half maximum (FWHM) of the EIT resonance [32]. We determined an upper bound  $\gamma_5 < 2\pi \times 80$  kHz by measuring the linewidth of this resonance at small Rabi couplings in a non-interacting gas. In the theoretical model, we fix  $\gamma_5$  to this measured upper bound.

3. **Dephasing due to the fluctuations of the single-photon probe detuning  $\Delta_p$ .** In our experiment, the major source of this non-Hermitian process is the uncertainty in the absolute laser frequency, which do not affect  $\delta$  because both the probe and control beams are derived from the same laser source. From the Hamiltonian (3), the Markovian fluctuations in the single-photon detuning will result in a jump operator of the form [3, 30, 31]

$$\hat{\mathcal{S}}_e^{\text{deph}} = \sqrt{\gamma_e}|e\rangle\langle e| \otimes \hat{I}^{\text{ext}}, \quad (7)$$

which projects the internal state to  $|e\rangle$  while not influencing the external state. The probability of an occurrence of this jump during the differential time  $dt$  is  $dp_e^{\text{deph}} = dt \langle \Psi | (\hat{\mathcal{S}}_e^{\text{deph}})^\dagger \hat{\mathcal{S}}_e^{\text{deph}} | \Psi \rangle = \gamma_e |\alpha_e|^2 dt$ . We fix this dephasing rate in the model to the typical standard deviation of the laser frequency (locked with a wavelength meter)  $\gamma_e \sim 2\pi \times 1.5$  MHz.

#### Conditioned state evolution after jump processes

Conditioned on not losing the atoms from the system (no spontaneous emission events (4) and (5)), the atom will be in one of the following states after the time evolution  $dt$ :

1. **Evolution without any jump:** With probability  $\mathcal{P}_1 = (1 - dp_5^{\text{deph}})(1 - dp_e^{\text{deph}})$ , the atom will not

undergo any dephasing (6) and (7). Under this condition, the state of the atom can be calculated with the non-Hermitian evolution

$$|\Psi_1(t+dt)\rangle = \zeta \left[ 1 - \frac{i}{\hbar} dt (\hat{H} - \frac{i\hbar}{2} \sum_j \hat{\mathcal{S}}_j^\dagger \hat{\mathcal{S}}_j) \right] |\Psi(t)\rangle, \quad (8)$$

where  $S_j$  are the jump operators (4), (5), (6), and (7) and  $\zeta$  is a normalization constant. Note that although we condition the problem on no spontaneous emission events (4) and (5), the projective nature of the absence of these events appears in the non-Hermitian contributions in the evolution (8). In fact, since our experimental parameters are in the limit of  $\Gamma_e \gg \Omega_p$ , this projective nature results in a reduction of the particle loss due to the continuous quantum Zeno effect [33]. One can show that

$$\zeta = \prod_j \frac{1}{\sqrt{1 - dp_j}}, \quad (9)$$

where  $dp_j$  denotes the probability of the occurrence of each jump process. By inserting all the jump operators in equation (8), the state of the atom is of the form  $|\Psi_1(t+dt)\rangle = |\phi_1(t+dt)\rangle \otimes |\phi_{\text{ext}}^{\text{(in)}}(t+dt)\rangle$  where the atom survives in the system ( $|\phi_{\text{ext}}^{\text{(in)}}(t+dt)\rangle \in S_{\text{in}}$ ). The resulting form of the internal state is:

$$|\phi_1(t+dt)\rangle = \zeta \left[ |\phi(t)\rangle - \frac{i}{\hbar} \hat{H}_{\text{in}} |\phi(t)\rangle - \frac{\gamma_5}{2} \alpha_5 |5\rangle - \frac{\Gamma_e + \gamma_e}{2} \alpha_e |e\rangle \right], \quad (10)$$

with  $\Gamma_e = \Gamma_{e1} + \Gamma_{e5}$ , the total linewidth of the excited state.

2. **A jump due to two-photon dephasing:** With probability  $\mathcal{P}_2 = dp_5^{\text{deph}}$ , the atom will undergo the dephasing jump (6), after which it will collapse to the state

$$|\Psi_2(t+dt)\rangle = \underbrace{|5\rangle}_{|\phi_2\rangle} \otimes |\phi_{\text{ext}}^{\text{(in)}}(t+dt)\rangle. \quad (11)$$

3. **A jump due to single-photon dephasing:** With probability  $\mathcal{P}_3 = dp_e^{\text{deph}}$ , the atom will undergo the dephasing jump (7) and collapses to the state

$$|\Psi_3(t+dt)\rangle = \underbrace{|e\rangle}_{|\phi_3\rangle} \otimes |\phi_{\text{ext}}^{\text{(in)}}(t+dt)\rangle. \quad (12)$$

4. **Simultaneous jumps of both single and two-photon dephasing:** Both of the jump events (6)



and (7) can happen simultaneously with the probability  $\mathcal{P}_4 = dp_5^{\text{deph}} dp_e^{\text{deph}}$ . However, since both  $dp_5^{\text{deph}}$  and  $dp_e^{\text{deph}}$  are of order  $dt$ , the probability  $\mathcal{P}_4$  will be of order  $dt^2$  and is neglected.

*Master equation of the surviving atom*

After the time evolution  $dt$ , the state of the system conditioned on survival inside the trap will be the statistical mixture of the internal part of states (8), (11), and (12):

$$\hat{\rho}(t+dt) = \mathcal{P}_1|\phi_1\rangle\langle\phi_1| + \mathcal{P}_2|\phi_2\rangle\langle\phi_2| + \mathcal{P}_3|\phi_3\rangle\langle\phi_3|. \quad (13)$$

At time  $t$  the density matrix of the system is of the form  $\rho(t) = |\phi(t)\rangle\langle\phi(t)|$ . Inserting the results discussed above in (13) and only keeping the terms linear in  $dt$  we get

$$\hat{\rho}(t+dt) = \frac{1}{1 - \Gamma_e \rho_{ee} dt} \left[ \hat{\rho}(t) + \mathcal{L}^{\text{tot}} \{ \hat{\rho}(t) \} dt \right] \quad (14)$$

with the total linear super-operator acting on the density matrix:

$$\mathcal{L}^{\text{tot}} \{ \hat{\rho} \} = -\frac{i}{\hbar} [\hat{H}_{\text{in}}, \hat{\rho}] + \mathcal{L}^{\text{spont}} \{ \hat{\rho} \} \quad (15)$$

$$+ \mathcal{L}_5^{\text{deph}} \{ \hat{\rho} \} + \mathcal{L}_e^{\text{deph}} \{ \hat{\rho} \}, \quad (16)$$

in which the first term captures the Hermitian evolution and the non-Hermitian super-operators act as

$$\mathcal{L}^{\text{spont}} \{ \hat{\rho} \} = \begin{pmatrix} 0 & 0 & -\frac{\Gamma_e}{2} \rho_{1e} \\ 0 & 0 & -\frac{\Gamma_e}{2} \rho_{5e} \\ -\frac{\Gamma_e}{2} \rho_{e1} & -\frac{\Gamma_e}{2} \rho_{e5} & -\Gamma_e \rho_{ee} \end{pmatrix}, \quad (17)$$

$$\mathcal{L}_5^{\text{deph}} \{ \hat{\rho} \} = \begin{pmatrix} 0 & -\frac{\gamma_5}{2} \rho_{15} & 0 \\ -\frac{\gamma_5}{2} \rho_{51} & 0 & -\frac{\gamma_5}{2} \rho_{5e} \\ 0 & -\frac{\gamma_5}{2} \rho_{e5} & 0 \end{pmatrix}, \quad (18)$$

$$\mathcal{L}_e^{\text{deph}} \{ \hat{\rho} \} = \begin{pmatrix} 0 & 0 & -\frac{\gamma_e}{2} \rho_{1e} \\ 0 & 0 & -\frac{\gamma_e}{2} \rho_{5e} \\ -\frac{\gamma_e}{2} \rho_{e1} & -\frac{\gamma_e}{2} \rho_{e5} & 0 \end{pmatrix}. \quad (19)$$

We note that the super-operator  $\mathcal{L}^{\text{spont}}$ , corresponding to the spontaneous emission through the excited state is not a trace-preserving operator. Due to the fact that we conditioned the evolution on the absence of spontaneous emission, the prefactor before the square bracket in (14) normalizes the loss of population due to  $\mathcal{L}^{\text{spont}}$ . This factor is reminiscent of the factor (9). By keeping only the linear terms in  $dt$  in (14), we obtain the master equation

$$\boxed{\frac{d\hat{\rho}}{dt} = \mathcal{L}^{\text{tot}} \{ \hat{\rho} \} + \Gamma_e \rho_{ee} \hat{\rho}}. \quad (20)$$

Note that we derived this evolution equation with the assumption that at time  $t$  the atom is in a pure internal state. We can use the linearity of the operator  $\mathcal{L}^{\text{tot}}$  in (14) to show the validity of the result (20) for the density matrix of a general mixed state.

## B. Numerical treatment of the evolution

To treat the time-dependent state of the atom, we use the master equation

$$\frac{d\hat{\rho}_{\text{tot}}}{dt} = \frac{1}{i\hbar} [\hat{H}, \hat{\rho}_{\text{tot}}] + \sum_j \left( \hat{S}_j \hat{\rho}_{\text{tot}} \hat{S}_j^\dagger - \frac{1}{2} \{ \hat{S}_j^\dagger \hat{S}_j, \hat{\rho}_{\text{tot}} \} \right), \quad (21)$$

in which the total density matrix is of the  $6 \times 6$  form

$$\hat{\rho}_{\text{tot}} = \begin{pmatrix} \hat{\rho}_{\text{in}} & \hat{\rho}_{\text{coh}} \\ \hat{\rho}_{\text{coh}}^\dagger & \hat{\rho}_{\text{out}} \end{pmatrix}, \quad (22)$$

where  $\hat{\rho}_{\text{in}}$  ( $\hat{\rho}_{\text{out}}$ ) is the  $3 \times 3$  internal state density matrix of the atom that survives (is lost) considering the possibility of spontaneous emission events. Furthermore, the off-diagonal  $3 \times 3$  matrix  $\hat{\rho}_{\text{coh}}$  accounts for the quantum coherence between the survived and lost parts of the motional state of the atom. Because the atom is initially purely inside the system ( $\hat{\rho}_{\text{out}} = 0$ ) and since the only process that can result in particle loss is spontaneous emission [jumps (4) and (5)], we can deduce that for all times  $\hat{\rho}_{\text{coh}} = 0$ . Here, we only consider the evolution of  $\hat{\rho}_{\text{in}}$ , which is independent of  $\hat{H}'_\Lambda$ . Therefore, this Hamiltonian is irrelevant and we set  $\hat{H}'_\Lambda = 0$ . We numerically solve the evolution equation (21) using the linear MCWF propagation tool provided by the python package *qutip* [34]. In this way, we extract the normalized density matrix of the survived atoms at each time step by

$$\hat{\rho}(t) = \frac{\hat{\rho}_{\text{in}}(t)}{\text{Tr}\{\hat{\rho}_{\text{in}}(t)\}}. \quad (23)$$

Although we discussed the derivation of (20) using MCWF approach above, we note that another method of deriving this master equation is by inserting the explicit form of the jump operators and the Hamiltonian in (21) and calculating the time evolution of the normalized density matrix (23) [29, 30].

## C. Analytic treatment of the steady state

The master equation of the  $\Lambda$  system in the absence of particle loss is linear [3]. In contrast, we see that the formulation of this loss results in a second order evolution equation (20). Here, we aim for an analytic, steady-state solution for the atoms that remain in the system. In our experiment we have a low probe coupling such that  $\Omega_p/\Gamma_e \ll 1$ . To solve the problem in this regime, we first write the evolution equation in a dimensionless form by dividing it by  $\Gamma_e$ . Then we solve it to the lowest order in  $\Omega_p/\Gamma_e$  using Wolfram Mathematica. The analytic solutions are presented in section VI.

## D. Validity of the steady state solution

As in our model the loss of an atom can be triggered by any scattering event, we can write the particle loss

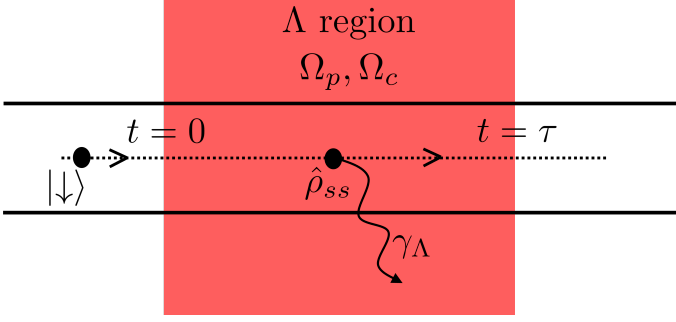


FIG. S1. A schematic of the transport of an atom inside the 1D channel which is initially in state  $|\downarrow\rangle$  through the  $\Lambda$  region (shown in red). In the  $\Lambda$  region, the coupling to common-mode probe and control beams is modelled by effective constant Rabi frequencies  $\Omega_p$  and  $\Omega_c$  respectively. The total flight time is denoted by  $\tau$ . The particle loss rate of the atom inside the coupling region is modeled by scattering rate  $\gamma_\Lambda$  defined in (24) for the steady state  $\hat{\rho}_{ss}$  of the survived atom calculated from the master equation (20). We adopted this steady state solution as the convergence time  $t_c$  is much shorter than the flight time  $\tau$  (see section ID).

rate of the atoms initially in  $|\downarrow\rangle$  as

$$\gamma_\Lambda = \Gamma_e \rho_{ee}. \quad (24)$$

Since we are most interested in this loss rate (see section II), we assess the convergence time of the density matrix element  $\rho_{ee}$  to its steady state. With the convergence criterion  $\rho_{ee}(t+dt) - \rho_{ee}(t) < 10^{-6}$ , we see that the numerical result converges to the analytic steady state solution with a time constant with an upper bound  $t_c < 5 \mu\text{s}$  in all experimental parameter regimes discussed in this work. To justify the use of the steady state solution, we compare this time scale with a lower bound of the total time the atom spends in the  $\Lambda$  region. In our cold Fermi gas, the velocity of the fastest atoms is on the order of the Fermi velocity  $v_F = \sqrt{2E_F/m} \approx 33.6 \mu\text{m/ms}$ . On the other hand, the length of the  $\Lambda$  region can be estimated using the measured  $1/e^2$  waist (see section VA):  $d \sim 2w_y \approx 3 \mu\text{m}$ . Therefore, a lower bound of the flight time of the atom through the  $\Lambda$  region is  $\tau > d/v_F \approx 91 \mu\text{s}$  showing  $\tau \gg t_c$ . Hence, in the majority of the flight time through the beams, the scattering rate obeys the steady state solution. We mention that the local chemical potential in the transport channel could be much smaller than  $v_F$ , which we calculated from  $E_F$  in the harmonic reservoirs. Therefore,  $\tau$  could assume much larger values than  $d/v_F$  as we also see from the result of section III.

## II. PHENOMENOLOGICAL MODEL OF TRANSPORT THROUGH CHANNEL

In this section, we formulate a model of transport of atoms through the quasi-1D channel incorporating the local  $\Lambda$  coupling. The result of this model is used in the

next section to fit the measured EIT spectra. In this formulation, the transport of atoms is modeled classically with the average flight time  $\tau$  through the  $\Lambda$  region. Furthermore, here, we simplify the problem by assuming that each  $|\downarrow\rangle$  atom experiences a constant effective Rabi coupling  $\Omega_p$  ( $\Omega_c$ ) of the probe (control) beam during the flight. The particle loss rate induced by the  $\Lambda$  system during the flight time is modeled by  $\gamma_\Lambda$  calculated from the steady state solution of (20) (see section ID). A schematic of our model is illustrated in Fig. S1. The time evolution of the probability of survival in the  $\Lambda$  region obeys

$$\frac{dp_\downarrow}{dt} = -(\gamma_\Lambda + \gamma_{\text{pair}})p_\downarrow, \quad (25)$$

$$\frac{dp_\uparrow}{dt} = -(r_{\text{spin}}\gamma_\Lambda + \gamma_{\text{pair}})p_\uparrow, \quad (26)$$

$$p_\downarrow(0) = p_\uparrow(0) = 1, \quad (27)$$

where  $p_\downarrow$  ( $p_\uparrow$ ) is the probability of survival of the atom in state  $|\downarrow\rangle$  ( $|\uparrow\rangle$ ) up to time  $t$  during the passage. We assume initial probabilities of one since the atoms enter the  $\Lambda$  region as a pure state in either of the spins. The parameter  $\gamma_{\text{pair}}$  is the rate of pair losses, originating in the off-resonant photoassociations induced by the control beam (see section VC). Furthermore, although  $\gamma_\Lambda$  originates from a  $\Lambda$  configuration that does not address atoms in state  $|\uparrow\rangle$ , due to strong interaction between  $|\downarrow\rangle$  and  $|\uparrow\rangle$ , each spin-selective loss of  $|\downarrow\rangle$  results in a probabilistic loss of atoms in state  $|\uparrow\rangle$  [35] modeled with the ratio  $r_{\text{spin}}$ . Due to the small singlet scattering length in  ${}^6\text{Li}$  [36, 37], we neglect the interaction in combinations  $|\downarrow\rangle - |\text{aux}\rangle$  (1-5) and  $|\uparrow\rangle - |\text{aux}\rangle$  (3-5), similar to the reported 2-6 [38] and 1-4 [39] scattering. By integrating the equations (25) and (26) we get the survival probabilities at the exit time  $t = \tau$ :

$$p_\downarrow(\tau) = e^{-(\gamma_\Lambda + \gamma_{\text{pair}})\tau}, \quad (28)$$

$$p_\uparrow(\tau) = 1 - \frac{r_{\text{spin}}\gamma_\Lambda + \gamma_{\text{pair}}}{\gamma_\Lambda + \gamma_{\text{pair}}} (1 - e^{-(\gamma_\Lambda + \gamma_{\text{pair}})\tau}). \quad (29)$$

In the absence of  $\Lambda$  couplings, we use the notation  $N_{\text{tot}}^{(\downarrow/\uparrow)}$  to indicate the total atom number in the cloud for each spin state. Furthermore, we denote the number of the atoms entering the  $\Lambda$ -region during the beams' total illumination time, which is the same as the transport time  $t$ , by  $N_{\text{pass}}^{(\downarrow/\uparrow)}$  for each state. We assume that it is a fraction of the total atom number given by a spin-independent and time-dependent phenomenological coefficient  $f_{\text{pass}}$ :

$$N_{\text{pass}}^{(\downarrow/\uparrow)} = f_{\text{pass}}(t)N_{\text{tot}}^{(\downarrow/\uparrow)}. \quad (30)$$

Multiplying  $N_{\text{pass}}^{(\downarrow/\uparrow)}$  by the loss probability through the channel  $1 - p_{\downarrow(\uparrow)}(\tau)$  from (28) and (29) results in the accumulated number of lost atoms in each spin state after the total illumination time. By subtracting this lost fraction from the total initial atom number and using (30),

we get the number of surviving atoms, measured at the end of the experiment:

$$N_{\downarrow}(t) = N_{\text{tot}}^{(\downarrow)} [1 - f_{\text{pass}}(t) (1 - p_{\downarrow}(\tau))], \quad (31)$$

$$N_{\uparrow}(t) = N_{\text{tot}}^{(\uparrow)} [1 - f_{\text{pass}}(t) (1 - p_{\uparrow}(\tau))]. \quad (32)$$

By introducing the initial spin ratio  $s_0 := N_{\text{tot}}^{(\downarrow)}/N_{\text{tot}}^{(\uparrow)}$ , dividing (31) by (32), and inserting (28) and (29), we arrive at the final result for the measured spin ratio  $s(t) = N_{\downarrow}(t)/N_{\uparrow}(t)$ :

$$s(t) = \frac{s_0 [1 - f_{\text{pass}}(t) (1 - e^{-(\gamma_{\Lambda} + \gamma_{\text{pair}})\tau})]}{1 - f_{\text{pass}}(t) \frac{r_{\text{spin}} \gamma_{\Lambda} + \gamma_{\text{pair}}}{\gamma_{\Lambda} + \gamma_{\text{pair}}} (1 - e^{-(\gamma_{\Lambda} + \gamma_{\text{pair}})\tau})}. \quad (33)$$

### III. FITTING PROCEDURES

For the loss spectroscopy of the dark state resonance, we use the equation (33) and fit it to the experimentally measured spin ratio after the illumination time  $t = 2$  s. The measurements are performed for six different control powers  $P_c$  with a common probe power  $P_p = 9.1(5)$  pW as illustrated in Fig. S2. We fix the ratio  $\frac{\Omega_c}{\Omega_p} = \frac{d_c}{d_p} \sqrt{\frac{P_c}{P_p}}$  in all of the data sets with  $d_p$  ( $d_c$ ) denoting the dipole element of the probe (control) atomic transition. The ratio of the dipole elements is  $d_c/d_p = \sqrt{\Gamma_{e5}/\Gamma_{e1}} = 18.51$ . Hence, during the fitting, all the control Rabi couplings  $\Omega_c$  are constrained to a function of a single free probe Rabi coupling  $\Omega_p$ . In (33), there are a few unknowns that are separately determined. As explained in subsection III A, the parameter  $r_{\text{spin}}$  is calibrated from separate measurements. Furthermore, in subsection III B,  $\gamma_{\text{pair}}$  and  $\tau$  are separately calibrated as functions of the fit parameter  $\Omega_p$ . We further fix  $s_0 = 1.03$  to the average value at  $t = 0$  from the transport data used in subsection III A. As discussed in section I the dephasing parameters of the processes (6) and (7) are fixed to  $\gamma_5 = 2\pi \times 0.08$  MHz and  $\gamma_e = 2\pi \times 1.5$  MHz respectively. Moreover,  $\Delta_p$  is calibrated by the observed loss resonance of this beam when the control power is zero. After using all these constraints and calibrations, the fitting is implemented with a minimal number of three free parameters:

$$\Omega_p, f_{\text{pass}}(t), \Delta_c. \quad (34)$$

We fit all six datasets simultaneously sharing the same fit parameters. The fit residual of each data point (mean value of 4-5 repetitions) is weighted by the inverse of the standard deviation (std) of the repetitions, while we set a maximum weight using the median std of all data points to improve fit stability. The results give a goodness of fit  $\chi_{\text{red}}^2 = 0.66$  and are shown in Fig. S2. From these results we presented three with control powers  $P_c \in \{14.6(8), 58(3), 178(10)\}$  pW in the main text (Fig. 2). The fitted parameters are  $\Omega_p = 2\pi \times 52(1)$  kHz,  $f_{\text{pass}}(t) = 0.653(5)$ ,  $\Delta_c = 2\pi \times 0.03(1)$  MHz. We mention that inserting  $\Omega_p$  in the calibrated relation (52) results in the light time  $\tau = 330(120)$   $\mu$ s.

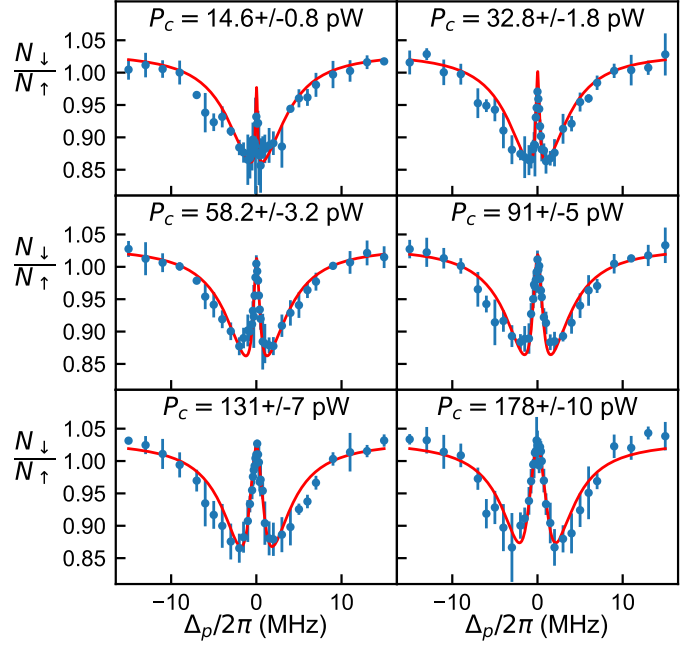


FIG. S2. Results of the fits for the observed EIT from the loss spectroscopy of the spin ratio after total illumination time  $t = 2$  s of the  $\Lambda$  beams. The calibrated power of the probe beam is  $P_p = 9.1(5)$  pW for all datasets with different control powers  $P_c$  (See section V A for the calibration of these powers). After applying physical constraints and experimental calibrations (see text), the fits are performed with three free parameters  $\Omega_p$ ,  $f_{\text{pass}}(t)$ , and  $\Delta_c$ .

#### A. Calibration of $r_{\text{spin}}$

To calibrate the parameter  $r_{\text{spin}}$ , we analyze measurements of the time evolution of  $N_{\downarrow}$  and  $N_{\uparrow}$  in short time limit when only the power of the probe beam is nonzero ( $P_c = 0$ ,  $P_p > 0$ ) and it is kept on resonance ( $\Delta_p = 0$ ). Since  $P_c = 0$ , the photoassociation loss is absent ( $\gamma_{\text{pair}} = 0$ ) and we can rewrite the survival probabilities (28) and (29) by

$$p_{\downarrow} = e^{-\gamma_{\text{pump}}\tau}, \quad (35)$$

$$p_{\uparrow} = 1 - r_{\text{spin}}(1 - e^{-\gamma_{\text{pump}}\tau}), \quad (36)$$

in which  $\gamma_{\Lambda}$  in the absence of the control beam is denoted by  $\gamma_{\text{pump}}$ . We note that this is the same particle loss mechanism due to optical pumping to state  $|\text{aux}\rangle$  used in [35] and the orange circles in Fig. 3. Moreover, in the short time limit, we assume that the number of atoms that enter the  $\Lambda$  region mentioned in (30) is linearly dependent on time:

$$f_{\text{pass}}(t) = f_0 t \Rightarrow N_{\text{pass}}^{(\downarrow/\uparrow)} = f_0 t \cdot N_{\text{tot}}^{(\downarrow/\uparrow)}. \quad (37)$$

By inserting equations (35), (36), and (37) into (31) and (32) we get the linearized equations for the atom number

evolution

$$N_{\downarrow}(t) = N_{\text{tot}}^{(\downarrow)}(1 - \xi t), \quad (38)$$

$$N_{\uparrow}(t) = N_{\text{tot}}^{(\uparrow)}(1 - r_{\text{spin}}\xi t), \quad (39)$$

where we defined

$$\xi = f_0(1 - e^{-\gamma_{\text{pump}}\tau}). \quad (40)$$

Therefore, we can rewrite the spin ratio in time:

$$s(t) = \frac{N_{\downarrow}(t)}{N_{\uparrow}(t)} = s_0 \frac{1 - \xi t}{1 - r_{\text{spin}}\xi t}. \quad (41)$$

To calibrate  $r_{\text{spin}}$ , we perform a two-step analysis. In the first step, we fit the equation (38) to the experimentally measured  $N_{\downarrow}$  for five data sets with distinct  $P_p$ . These fits are implemented with free parameters  $N_{\text{tot}}^{(\downarrow)}$  and  $\xi$  that are separately extracted for each set [Fig. S3(a)]. In the second step, we fit equation (41) to the spin ratio from the same measurements, with  $\xi$  fixed to the fit results from the first step. Furthermore,  $s_0 = 1.03(1)$  is fixed to the average spin ratio at  $t = 0$ . In the end, the fit is performed with a single free parameter  $r_{\text{spin}}$  common to all data sets. The fit results are presented in Fig. S3(b), with

$$r_{\text{spin}} = 0.63(2), \quad (42)$$

which is comparable to the value 0.72(4) calibrated with a different method in a previous work in a similar setting [35].

### B. Calibration of $\gamma_{\text{pair}}$ and $\tau$

The photoassociation pair loss rate  $\gamma_{\text{pair}}$  (introduced in section II) is modeled to be only a function of the control power,  $\gamma_{\text{pair}} \propto P_c$ . The goal is to calibrate this proportionality factor with experiments only having the control beam,  $P_p = 0$ ,  $P_c > 0$ , under which condition  $\gamma_{\Lambda} = 0$ . However, the transport setting introduces a few unknown factors (see below). The idea is then to compare the atom loss rate to that in the complementary condition  $P_p > 0$ ,  $P_c = 0$ , also in the same transport setting. In the latter condition, the scattering rate is determined by the theoretically known optical pumping rate of atoms from  $|\downarrow\rangle$  to  $|\text{aux}\rangle$  denoted by  $\gamma_{\text{pump}}$ . Therefore we can relate  $\gamma_{\text{pair}}$  to  $\gamma_{\text{pump}}$ , hence to the laser powers. Since we are working in the limit  $\Omega_p \ll \Gamma_e$ ,  $\gamma_{\text{pump}}$  is given by (see equations (73) for the case of  $\Omega_c = 0$ ,  $\Delta_p = 0$  and the discussion of continuous quantum Zeno effect in [33]):

$$\gamma_{\text{pump}} = \frac{\Omega_p^2}{\Gamma_e + \gamma_e}, \quad (43)$$

where we can see  $\gamma_{\text{pump}} \propto P_p$ . Given that  $\gamma_{\text{pair}} \propto P_c$ , it can be expressed as

$$\gamma_{\text{pair}}(P_c) = \alpha(P_c/P_p)\gamma_{\text{pump}}(P_p), \quad (44)$$

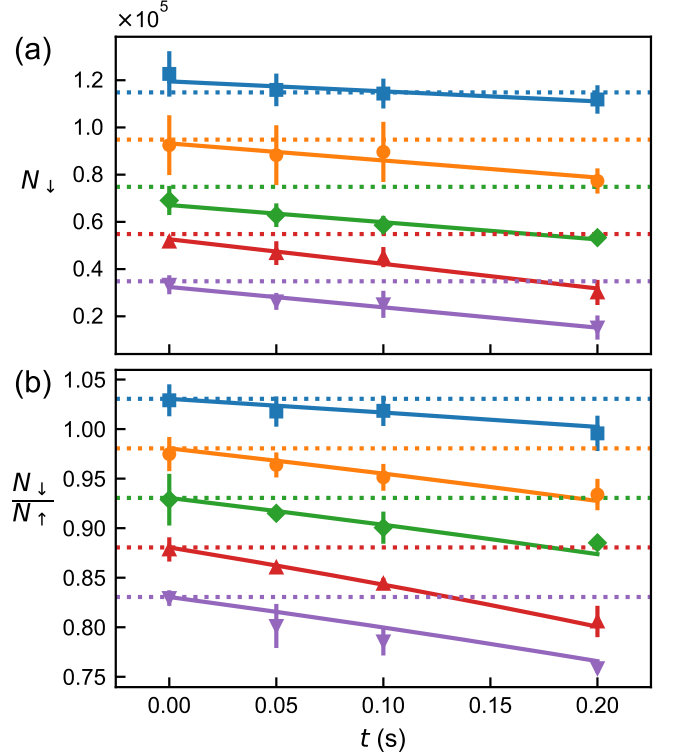


FIG. S3. The calibration procedure of the constant  $r_{\text{spin}}$ . Here, we investigate the short time evolution of the system where only probe beam is present ( $P_p > 0$ ,  $P_c = 0$ ). In each panel the probe power is set to  $P_p = 14.6(8)$ ,  $33(2)$ ,  $58(3)$ ,  $91(5)$ ,  $131(7)$  pW, top to bottom respectively. (a) In the first step, equation (38) is fitted over  $N_{\downarrow}$  to extract  $N_{\text{tot}}^{(\downarrow)}$  and  $\xi$  for each data set. For clarity, the results for different sets are shifted downward vertically. The dashed lines represent the baseline of each curve: the average measured initial atom number  $N_{\downarrow}(t = 0) = 1.2(1) \times 10^5$ . (b) In the second step, we fit equation (41) to all the data sets simultaneously, with a single free parameter  $r_{\text{spin}}$ , see text. For clarity, different datasets are shifted downward in the increasing order of  $P_p$ . For each curve, the dashed lines represent the measured baseline  $s_0 = 1.03(1)$ . The final fit result is  $r_{\text{spin}} = 0.63(2)$ .

where  $\alpha$  is the proportionality factor that we aim to experimentally calibrate. This is done in three steps as follows.

#### Step 1

In the first step, we use the measured atom number evolution with condition  $P_p = 0$  and  $P_c > 0$ . Under this condition, the probability of survival of atoms in both states from equations (29) and (28) reduces to

$$p_{\downarrow} = p_{\uparrow} = e^{-\gamma_{\text{pair}}\tau}. \quad (45)$$



Due to the equal loss rate in both spins, here we choose to only analyze the evolution of the atom number in state  $|\uparrow\rangle$ . With the help of equation (32) and by assuming linear relation (37) for the short time limit, we arrive at

$$N_{\uparrow}(t) = N_{\text{tot}}^{(t)}(1 - \eta t), \quad (46)$$

in which we defined

$$\eta = f_0(1 - e^{-\gamma_{\text{pair}}\tau}). \quad (47)$$

We extract the parameters  $N_{\text{tot}}^{(t)}$  and  $\eta$  from fitting separately to the measurements of  $N_{\uparrow}$  with each  $P_c$  setting for  $t \leq 1$  s. Results are presented in Fig. S4(a), showing that the linearization (37) is justified in this regime. As  $f_0$  and  $\tau$  are unknown, it requires additional data to determine  $\gamma_{\text{pair}}$ .

### Step 2

In the second step, we use the data set with the lowest probe power  $P_p = 14.6(8)$  pW (defined as  $P_p^*$ ) and  $P_c = 0$ . This is the same data set presented as blue squares in Fig. S3. Due to the weak power of the probe beam, we use all the measured time points up to  $t = 1$  s (not all shown in Fig. S3), which fall in the linear evolution regime (38). By fitting equation (38) as discussed in section III A, we extract the parameter  $\xi(P_p^*) = 0.39(2)$ . We also define the corresponding loss rate as  $\gamma_{\text{pump}}^*$ . Therefore, from (44),  $\gamma_{\text{pair}}$  can be written as

$$\gamma_{\text{pair}} = \alpha \gamma_{\text{pump}}^* P_c / P_p^* \quad (48)$$

### Step 3

Within our model, we assume that  $f_0$  and  $\tau$  in  $\xi$  of (40) are the same as those in  $\eta$  of (47). Therefore, from the previously fitted  $\eta(P_c)$  (step 1) and  $\xi(P_p^*)$  (step 2), we can eliminate the unknown factor  $f_0$  and obtain

$$\frac{\eta(P_c)}{\xi(P_p^*)} = \frac{1 - e^{-\gamma_{\text{pair}}\tau}}{1 - e^{-\gamma_{\text{pump}}^*\tau}} = \frac{1 - e^{-A^* \cdot \alpha P_c / P_p^*}}{1 - e^{-A^*}}, \quad (49)$$

where we defined  $A^* := \gamma_{\text{pump}}^*\tau$  and used (48). We use equation (49) and fit it to the obtained  $\eta(P_c)$  from step 1 as a function of  $P_c$  [see Fig. S4 (b)], which results in

$$\boxed{\alpha = 0.086(8)}, \quad \boxed{A^* = 1.2(4)}. \quad (50)$$

We can rewrite the equation (44) by using (43) for general power settings:

$$\gamma_{\text{pair}}(P_c) = \alpha \frac{P_c}{P_p} \frac{\Omega_p^2}{\Gamma_e + \gamma_e}, \quad (51)$$

in which  $\Omega_p$  is the probe Rabi frequency corresponding to the chosen power  $P_p$ . In this way, we calibrate  $\gamma_{\text{pair}}$  in

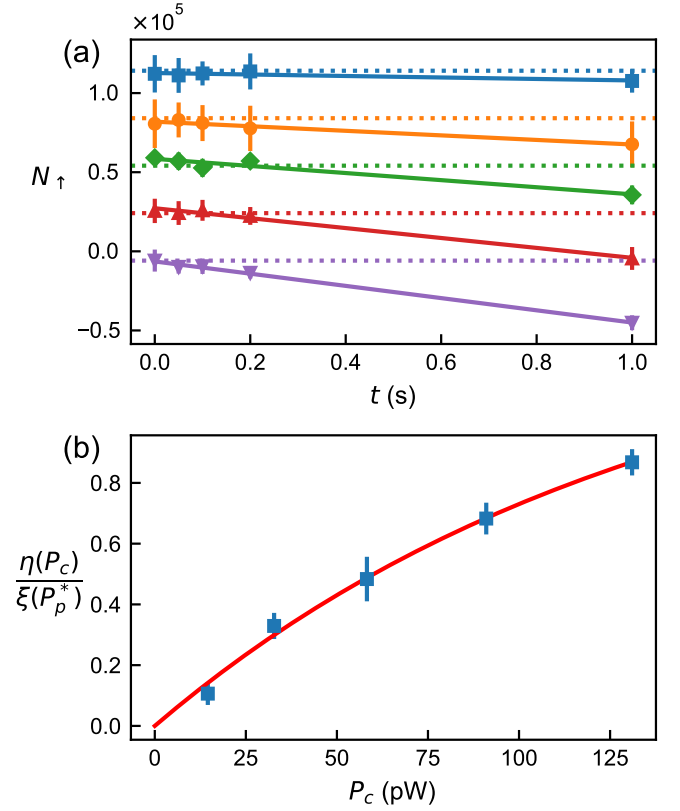


FIG. S4. The calibration procedure for the pair loss  $\gamma_{\text{pair}}$ . (a) Analysis of the atom number for  $|\uparrow\rangle$  atoms for the power settings  $P_p = 0$  and  $P_c = 14.6(8), 33(2), 58(3), 91(5), 131(7)$  pW in the increasing order from top to bottom. Except for the smallest  $P_c$  (blue square), other datasets are shifted for clarity. The dashed line for each set is the reference atom number fixed to the average  $N_{\uparrow} = 1.1(1) \times 10^5$  calculated over all datasets at  $t = 0$ . By fitting the linear equation (46) over each dataset separately, we extract the parameters  $\eta$  and  $N_{\text{tot}}^{(t)}$  for each  $P_c$  setting. (b) Ratio  $\eta(P_c)/\xi(P_p^*)$  for each  $P_c$ , with  $\xi(P_p^*)$  extracted from the linear regime ( $t \leq 1$  s) of the  $N_{\uparrow}$  evolution for the dataset with  $P_p^* = 14.6(8)$  pW and  $P_c = 0$  (same data set shown in blue square in Fig. S3). By fitting equation (49), we eventually relate  $\gamma_{\text{pair}}$  to beam powers, see text.

terms of the fit parameter of the full model,  $\Omega_p$ . We can also extract the flight time  $\tau$  from the fitted  $A^*$ . Again by using (43), we can rewrite it in terms of  $\Omega_p$  with

$$\tau = \frac{A^* P_p / P_p^*}{\Omega_p^2 / (\Gamma_e + \gamma_e)}. \quad (52)$$

We did check that leaving  $\tau$  as a free parameter in the final fit using (33) does not much influence the fit quality and has almost no influence on the obtained  $\Omega_p$  and  $\Omega_c$ . We therefore keep the fit as simple as possible by constraining  $\tau$  to  $\Omega_p$  using (52).

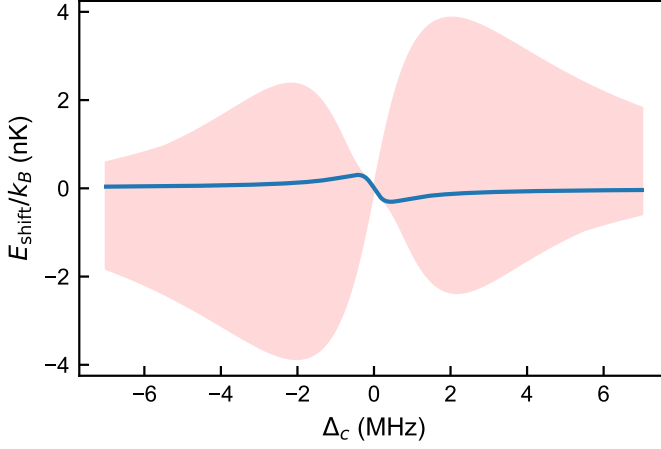


FIG. S5. The light shift (60) in terms of  $\Delta_c$  in the configuration of  $\Lambda$ -system parameters of the experiment of Fig. 4, red triangles. The solid blue line is the value of the light shift of the steady state solution of (20). The transient light shift before reaching the steady state explores the shaded red region.

#### IV. ESTIMATING DIPOLE POTENTIALS

Here we formulate the total dipole potential that an atom feels under the  $\Lambda$  coupling. In a general time-dependent rotating frame

$$|\tilde{\psi}\rangle = \hat{U}(t)|\psi\rangle, \quad (53)$$

where we denote the parameters in the rotating frame with  $\tilde{\phantom{x}}$  and the ones in the Schrödinger frame without, the Hamiltonian transforms as

$$\hat{\tilde{H}} = \hat{U}\hat{H}\hat{U}^\dagger + i\hbar\frac{d\hat{U}}{dt}\hat{U}^\dagger. \quad (54)$$

The energy shift of the atom in the state  $|\psi\rangle$  expressed in the Schrödinger frame is

$$E_{\text{shift}} = \langle\psi|\hat{\tilde{H}}|\psi\rangle - \langle\psi|\hat{H}_0|\psi\rangle, \quad (55)$$

in which  $H_0$  is the Hamiltonian of the atom in the absence of any light field. We can rewrite equation (55) using (53) and (54):

$$E_{\text{shift}} = \langle\tilde{\psi}|\hat{U}(\hat{H} - \hat{H}_0)\hat{U}^\dagger|\tilde{\psi}\rangle \quad (56)$$

$$= \langle\tilde{\psi}|\underbrace{\left(\hat{\tilde{H}} - i\hbar\frac{d\hat{U}}{dt}\hat{U}^\dagger - \hat{U}\hat{H}_0\hat{U}^\dagger\right)}_{\hat{H}'}|\tilde{\psi}\rangle. \quad (57)$$

Using the general density matrix  $\hat{\rho} = \sum_{j=1}^3 p_j |\tilde{\phi}_j\rangle\langle\tilde{\phi}_j|$  expressed in the rotating frame, we get the expression for the light shift:

$$E_{\text{shift}} = \text{Tr}\{\hat{H}'\hat{\rho}\}. \quad (58)$$

For the case of the three-level system in the rotating frame with Hamiltonian (3) and its corresponding time-dependent unitary operator we have

$$\hat{H}' = \hbar \begin{pmatrix} 0 & 0 & -\frac{\Omega_p}{2} \\ 0 & 0 & -\frac{\Omega_c}{2} \\ -\frac{\Omega_p}{2} & -\frac{\Omega_c}{2} & 0 \end{pmatrix}. \quad (59)$$

We see that this effective Hamiltonian used for the calculation of the light shift is independent of the detuning. However, the detuning could influence the state of the system  $\hat{\rho}$  which in turn affects  $E_{\text{shift}}$ . Inserting (59) in (58) results in

$$E_{\text{shift}} = -\hbar\Omega_p \text{Re}\{\rho_{1e}\} - \hbar\Omega_c \text{Re}\{\rho_{5e}\}. \quad (60)$$

Using the steady state solutions of (20) from section VI, we see that at the single-photon resonance ( $\Delta_p = 0$ , same condition as in Fig. 4), and in the limit of zero two-photon dephasing ( $\gamma_5 = 0$ ), we have  $E_{\text{shift}} = 0$  for all two-photon detunings  $\delta$  close to the resonance. As  $\gamma_5$  increases,  $E_{\text{shift}}$  deviates more from zero. To find a maximum bound for the magnitude of  $E_{\text{shift}}$ , we theoretically analyze this parameter for the case of the maximum bound of the two-photon dephasing in our experiment,  $\gamma_5 = 2\pi \times 80$  kHz. The results as a function of  $\Delta_c$  for  $\Lambda$  parameters  $\Omega_p = 2\pi \times 0.098$  MHz,  $\Omega_c = 2\pi \times 2.42$  MHz, and  $\Delta_p = 0$  (same setting as red triangles in Fig. 4) are presented in Fig. S5. Blue solid line shows the analytic steady state solution calculated by inserting (77) and (80) in (60). The shaded region shows maximum excursions of all transient values of  $E_{\text{shift}}$  the atom experiences before reaching the steady state. For this, the time-dependent value of the density matrix extracted by the numerical method discussed in section IB is inserted in (60). We see that the value of the light shift does not exceed  $k_B \cdot 4$  nK at all times. In comparison with other energy scales of the system such as temperature  $T = 80(1)$  nK, Fermi energy  $E_F = k_B \cdot 408(5)$  nK, transverse confinement energies of the channel (see section VB)  $\nu_x^{(\text{ch})} = k_B/h \cdot 592(11)$  nK,  $\nu_z^{(\text{ch})} = k_B/h \cdot 514(6)$  nK,  $E_{\text{shift}}$  is negligible, suggesting that the observed asymmetry in Fig. 4(a) does not originate from the light shift of the  $\Lambda$  system.

#### V. EXPERIMENTAL DETAILS

##### A. Calibration of Rabi frequencies by power measurements

To extract the intensity of the beams on the atoms, we image the beam profile and fit it to a 2D Gaussian function,

$$I(x, y) = \frac{2P_0}{\pi w_x w_y} e^{-\frac{2x^2}{w_x^2}} e^{-\frac{2y^2}{w_y^2}}, \quad (61)$$

where  $P_0$  is the beam power, resulting in the waists  $w_x = 1.38$   $\mu\text{m}$ ,  $w_y = 1.52$   $\mu\text{m}$ . The Rabi frequency is related to

the intensity via

$$\Omega/2\pi = \sqrt{\frac{2}{c\epsilon_0 h^2}} d_{ge} \sqrt{I}, \quad (62)$$

where  $c$  is the speed of light,  $\epsilon_0$  is the vacuum permittivity, and  $d_{ge}$  is the dipole moment, taking the values [41]

$$d_p = 1.073 \times 10^{-30} \text{ Cm}, \quad (63)$$

$$d_c = 1.985 \times 10^{-29} \text{ Cm}, \quad (64)$$

for the probe and control transitions respectively. With this, we calibrate the peak Rabi frequencies for each beam:

$$\Omega_p^{\text{peak}}/2\pi = 24.43(3) \text{ kHz} \cdot \sqrt{P_p [\text{pW}]}, \quad (65)$$

$$\Omega_c^{\text{peak}}/2\pi = 452.2(5) \text{ kHz} \cdot \sqrt{P_c [\text{pW}]}, \quad (66)$$

with  $P_p$  and  $P_c$  the power of the beams on the atomic cloud in the  $\sigma_+$  polarization expressed in pW. Here, we compare the calibrations (65) and (66) with the Rabi couplings resulted from the fit in Fig. 2. There, we experimentally fixed  $P_p = 9.1(5)$  pW which corresponds to  $\Omega_p^{\text{peak}} = 2\pi \times 74(2)$  kHz from (65). In the theoretical model that we used for the fit (see section II), the effective Rabi couplings are constant across the  $\Lambda$  region. Therefore, to compare with theory, we extract a constant Rabi coupling  $\bar{\Omega}_p$  by averaging the Gaussian profile of the measured intensity in a region with length  $2w_y$  along  $y$  direction. With this, we get  $\bar{\Omega}_p = 2\pi \times 58(2)$  kHz which is in good agreement with  $\Omega_p = 2\pi \times 52(1)$  kHz from the fit result of Fig. 2.

### B. Transport geometry and the experimental sequence

To create the potential landscape for the transport configuration, a cigar-shaped gas trapped in a hybrid magnetic and dipole trap with trapping frequencies  $\nu_x = 168(2)$  Hz,  $\nu_y = 28.18(4)$  Hz,  $\nu_z = 148(1)$  Hz is partitioned in two reservoirs using two TEM<sub>01</sub>-like repulsive beams which propagate along  $x$  and  $z$  directions as defined in Fig. 1. This results in a transport channel along the  $y$  direction between the two reservoirs with peak confinement frequencies  $\nu_x^{(\text{ch})} = 12.3(2)$  kHz,  $\nu_z^{(\text{ch})} = 10.7(1)$  kHz. Since these confinement energies are much larger than the reservoirs' average temperature  $k_B T/h = 1.67(3)$  kHz, the transport happens in the 1D regime. The length  $l = 6.9$   $\mu\text{m}$  of the 1D region is determined by the smallest waist along  $y$  of the TEM<sub>01</sub>-like beams. To tune the number of occupied transverse modes and the degeneracy in the channel, an attractive 767 nm *gate* beam covering the channel region is used. To fully block the transport through the channel, we use another repulsive *wall* beam propagating along  $z$  with an elliptical profile with a smaller waist along  $y$  centered at the channel. Starting from a particle number imbalance between

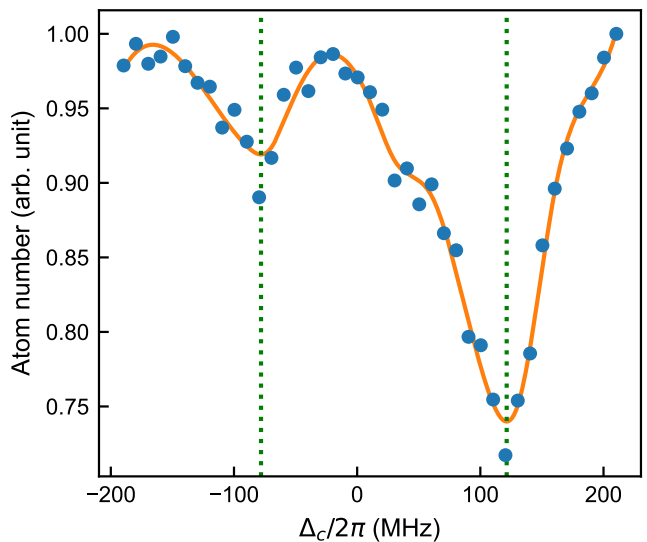


FIG. S6. Normalized photoassociation pair loss induced by the control beam alone. We observe mainly two resonances (shown in green dotted lines) at  $\Delta_c \sim 121$  MHz and  $\Delta_c \sim -78$  MHz. The orange solid line is an interpolation of the data points as a guide to the eye.

the two reservoirs with the wall beam blocking the transport, we switch off the wall for the time duration  $t$  after which it is switched back on. After ramping down all confinement beams to zero, we measure the density profile in each reservoir. In this way, we access the state of the reservoirs after transport time  $t$ . See [40] for more details on the experimental sequence and the transport geometry of this experiment.

### C. Photoassociation pair loss

In the unitary regime, we observe photoassociation pair losses [42, 43] induced by the control beam. The measured atom loss spectrum of only the control beam ( $P_p = 0$ ,  $P_c > 0$ ) is presented in Fig. S6. We observe mainly two broad resonances detuned from the  $|\text{aux}\rangle - |e\rangle$  resonance ( $\Delta_c = 0$ ). These measurements are performed with the control beam located in the reservoir to improve the signal to noise ratio.

## VI. ANALYTIC FORM OF THE STEADY-STATE OF THE DENSITY MATRIX OF THE SURVIVING ATOMS IN THE LIMIT $\Omega_p \ll \Gamma_e$

Here we present the analytic steady state solutions of the equation (20) in the limit  $\Omega_p \ll \Gamma_e$ . In the density matrix elements, the subscripts 1 and 5 correspond to the states  $|\downarrow\rangle$  and  $|\text{aux}\rangle$  respectively. The rest of the notations are all introduced in section I.

### A. Solutions in the general case

We first define the frequently appearing denominator notations

$$\mathbf{D}_a = (\gamma_5^2 + 4(\Delta_p - \Delta_c)^2) ((\gamma_e + \Gamma_e)^2 + 4\Delta_p^2) + 2\Omega_c^2 (\gamma_5 (\gamma_e + \Gamma_e) + 4\Delta_p (\Delta_c - \Delta_p)) + \Omega_c^4, \quad (67)$$

$$\mathbf{D}_b = (\gamma_5 + \gamma_e + \Gamma_e) \mathbf{D}_a. \quad (68)$$

The resulting density matrix elements follow

$$\rho_{11} = 1 - \frac{\mathbf{N}_{11}}{\mathbf{D}_b} \left( \frac{\Omega_p}{\Gamma_e} \right)^2 + \mathcal{O} \left[ \left( \frac{\Omega_p}{\Gamma_e} \right)^4 \right], \quad (69)$$

in which

$$\begin{aligned} \mathbf{N}_{11} = & \Gamma_e \left[ \gamma_5^2 ((\gamma_e + \Gamma_e)(2\gamma_e + 3\Gamma_e) + 2\Omega_c^2) + 2\gamma_5^3 (\gamma_e + \Gamma_e) + (\gamma_e + \Gamma_e) (4(2\gamma_e + \Gamma_e)(\Delta_p - \Delta_c)^2 + \Gamma_e \Omega_c^2) \right. \\ & \left. + \gamma_5 (\gamma_e^2 \Gamma_e + 2\gamma_e (\Gamma_e^2 + 4(\Delta_p - \Delta_c)^2 + \Omega_c^2) + \Gamma_e (\Gamma_e^2 + 4\Delta_p^2 - 8\Delta_p \Delta_c + 8\Delta_c^2 + 3\Omega_c^2)) \right]. \end{aligned} \quad (70)$$

$$\rho_{55} = \frac{\mathbf{N}_{55}}{\mathbf{D}_b} \left( \frac{\Omega_p}{\Gamma_e} \right)^2 + \mathcal{O} \left[ \left( \frac{\Omega_p}{\Gamma_e} \right)^4 \right], \quad (71)$$

in which

$$\begin{aligned} \mathbf{N}_{55} = & \Gamma_e \left[ \gamma_5^2 ((\gamma_e + \Gamma_e)(\gamma_e + 2\Gamma_e) + \Omega_c^2) + \gamma_5^3 (\gamma_e + \Gamma_e) + (\gamma_e + \Gamma_e) (4\gamma_e (\Delta_p - \Delta_c)^2 + \Gamma_e \Omega_c^2) \right. \\ & \left. + \gamma_5 (\gamma_e^2 \Gamma_e + \gamma_e (2\Gamma_e^2 + 4(\Delta_p - \Delta_c)^2 + \Omega_c^2) + \Gamma_e (\Gamma_e^2 + 4\Delta_c^2 + 2\Omega_c^2)) \right]. \end{aligned} \quad (72)$$

$$\rho_{ee} = \frac{\mathbf{N}_{ee}}{\mathbf{D}_a} \left( \frac{\Omega_p}{\Gamma_e} \right)^2 + \mathcal{O} \left[ \left( \frac{\Omega_p}{\Gamma_e} \right)^4 \right], \quad (73)$$

in which

$$\mathbf{N}_{ee} = \Gamma_e ((\gamma_e + \Gamma_e) (\gamma_5^2 + 4(\Delta_p - \Delta_c)^2) + \gamma_5 \Omega_c^2). \quad (74)$$

$$\text{Im}\{\rho_{e1}\} = \frac{\mathbf{N}_{e1}^{\text{Im}}}{\mathbf{D}_a} \left( \frac{\Omega_p}{\Gamma_e} \right) + \mathcal{O} \left[ \left( \frac{\Omega_p}{\Gamma_e} \right)^3 \right], \quad (75)$$

in which

$$\mathbf{N}_{e1}^{\text{Im}} = \Gamma_e ((\gamma_e + \Gamma_e) (\gamma_5^2 + 4(\Delta_p - \Delta_c)^2) + \gamma_5 \Omega_c^2). \quad (76)$$

$$\text{Re}\{\rho_{e1}\} = \frac{\mathbf{N}_{e1}^{\text{Re}}}{\mathbf{D}_a} \left( \frac{\Omega_p}{\Gamma_e} \right) + \mathcal{O} \left[ \left( \frac{\Omega_p}{\Gamma_e} \right)^3 \right], \quad (77)$$



in which

$$\mathbf{N}_{e1}^{\text{Re}} = 2\Gamma_e (\Delta_p (\gamma_5^2 + 4(\Delta_p - \Delta_c)^2) + \Omega_c^2(\Delta_c - \Delta_p)). \quad (78)$$

$$\text{Im}\{\rho_{e5}\} = 0 + \text{O}\left[\left(\frac{\Omega_p}{\Gamma_e}\right)^4\right]. \quad (79)$$

$$\text{Re}\{\rho_{e5}\} = \frac{\mathbf{N}_{e5}^{\text{Re}}}{\mathbf{D}_b} \left(\frac{\Omega_p}{\Gamma_e}\right)^2 + \text{O}\left[\left(\frac{\Omega_p}{\Gamma_e}\right)^4\right], \quad (80)$$

in which

$$\mathbf{N}_{e5}^{\text{Re}} = 2\Gamma_e^2 \Omega_c (\gamma_5 \Delta_p + (\gamma_e + \Gamma_e)(\Delta_p - \Delta_c)). \quad (81)$$

$$\text{Im}\{\rho_{51}\} = \frac{\mathbf{N}_{51}^{\text{Im}}}{\mathbf{D}_a} \left(\frac{\Omega_p}{\Gamma_e}\right) + \text{O}\left[\left(\frac{\Omega_p}{\Gamma_e}\right)^3\right], \quad (82)$$

in which

$$\mathbf{N}_{51}^{\text{Im}} = 2\Gamma_e \Omega_c (\gamma_5 \Delta_p + (\gamma_e + \Gamma_e)(\Delta_p - \Delta_c)). \quad (83)$$

$$\text{Re}\{\rho_{51}\} = \frac{\mathbf{N}_{51}^{\text{Re}}}{\mathbf{D}_a} \left(\frac{\Omega_p}{\Gamma_e}\right) + \text{O}\left[\left(\frac{\Omega_p}{\Gamma_e}\right)^3\right], \quad (84)$$

in which

$$\mathbf{N}_{51}^{\text{Re}} = -\Gamma_e \Omega_c (\gamma_5 (\gamma_e + \Gamma_e) + 4\Delta_p (\Delta_c - \Delta_p) + \Omega_c^2). \quad (85)$$

## B. Solutions in the case of zero dephasing

Here we simplify the results of the previous subsection for the case of zero dephasing  $\gamma_5 = \gamma_e = 0$ . We first define the frequently recurring denominator notation

$$\mathbf{D} = 4\Gamma_e^2 (\Delta_p - \Delta_c)^2 + (4\Delta_p (\Delta_c - \Delta_p) + \Omega_c^2)^2. \quad (86)$$

The resulting density matrix elements follow:

$$\rho_{11} = 1 - \frac{\Gamma_e^2 (4(\Delta_p - \Delta_c)^2 + \Omega_c^2)}{\mathbf{D}} \left(\frac{\Omega_p}{\Gamma_e}\right)^2 + \text{O}\left[\left(\frac{\Omega_p}{\Gamma_e}\right)^4\right], \quad (87)$$

$$\rho_{55} = \frac{\Gamma_e^2 \Omega_c^2}{\mathbf{D}} \left(\frac{\Omega_p}{\Gamma_e}\right)^2 + \text{O}\left[\left(\frac{\Omega_p}{\Gamma_e}\right)^4\right], \quad (88)$$

$$\rho_{ee} = \frac{4\Gamma_e^2 (\Delta_p - \Delta_c)^2}{\mathbf{D}} \left(\frac{\Omega_p}{\Gamma_e}\right)^2 + \text{O}\left[\left(\frac{\Omega_p}{\Gamma_e}\right)^4\right], \quad (89)$$

$$\text{Im}\{\rho_{e1}\} = \frac{4\Gamma_e^2 (\Delta_p - \Delta_c)^2}{\mathbf{D}} \left(\frac{\Omega_p}{\Gamma_e}\right) + \text{O}\left[\left(\frac{\Omega_p}{\Gamma_e}\right)^3\right], \quad (90)$$

$$\operatorname{Re}\{\rho_{e1}\} = \frac{2\Gamma_e(\Delta_p - \Delta_c)(4\Delta_p(\Delta_p - \Delta_c) - \Omega_c^2)}{\mathbf{D}} \left(\frac{\Omega_p}{\Gamma_e}\right) + \mathcal{O}\left[\left(\frac{\Omega_p}{\Gamma_e}\right)^3\right], \quad (91)$$

$$\operatorname{Im}\{\rho_{e5}\} = 0 + \mathcal{O}\left[\left(\frac{\Omega_p}{\Gamma_e}\right)^4\right], \quad (92)$$

$$\operatorname{Re}\{\rho_{e5}\} = \frac{2\Gamma_e^2\Omega_c(\Delta_p - \Delta_c)}{\mathbf{D}} \left(\frac{\Omega_p}{\Gamma_e}\right)^2 + \mathcal{O}\left[\left(\frac{\Omega_p}{\Gamma_e}\right)^4\right], \quad (93)$$

$$\operatorname{Im}\{\rho_{51}\} = \frac{2\Gamma_e^2\Omega_c(\Delta_p - \Delta_c)}{\mathbf{D}} \left(\frac{\Omega_p}{\Gamma_e}\right) + \mathcal{O}\left[\left(\frac{\Omega_p}{\Gamma_e}\right)^3\right], \quad (94)$$

$$\operatorname{Re}\{\rho_{51}\} = -\frac{\Gamma_e\Omega_c(4\Delta_p(\Delta_c - \Delta_p) + \Omega_c^2)}{\mathbf{D}} \left(\frac{\Omega_p}{\Gamma_e}\right) + \mathcal{O}\left[\left(\frac{\Omega_p}{\Gamma_e}\right)^3\right]. \quad (95)$$